NACA TN 3555

NATIONAL ADVISORY COMMITTEE FOR AERONAUTICS

TECHNICAL NOTE 3555

A METHOD FOR CALCULATING THE CONTOUR OF BODIES OF REVOLUTION WITH A PRESCRIBED PRESSURE GRADIENT AT SUPERSONIC SPEED WITH EXPERIMENTAL VERIFICATION

By Paige B. Burbank

Langley Aeronautical Laboratory
Langley Field, Va.

Washington
March 1956

W

NATIONAL ADVISORY COMMITTEE FOR AERONAUTICS

TECHNICAL NOTE 3555

A METHOD FOR CALCULATING THE CONTOUR OF BODIES OF REVOLUTION WITH A PRESCRIBED PRESSURE GRADIENT AT SUPERSONIC SPEED WITH EXPERIMENTAL VERIFICATION

By Paige B. Burbank

SUMMARY

A method based upon the theory of characteristics has been developed to compute the contour of a body for a prescribed pressure distribution. An indication of the accuracy of the method was obtained by using the pressure distribution which had been determined by the conventional method of characteristics to compute the ordinates near the nose of a body. The agreement between the original and computed ordinates was good. A model was constructed with an initial included cone angle of 30° and a contour to give a linear pressure distribution for a free-stream Mach number of 3.13. Good agreement between the experimental and computed pressure distributions was obtained when the model was tested at free-stream Mach numbers of 3.05 and 3.13.

INTRODUCTION

In the past, no method that permits computation of a body of revolution with a particular pressure distribution has been available. The design of such a body would be useful in the investigation of many aerodynamic problems such as those associated with body-wing interaction, inlets, and boundary-layer transition, separation, and shock interaction. In this paper, a method based upon the theory of characteristics has been developed to compute the contour of a body for a prescribed pressure distribution. This method has been used to compute the contour of a body which has a constant pressure gradient. This pressure distribution was chosen since the theoretical approach to the problem of transition indicates that it would be desirable to have, for certain experimental studies, a constant pressure gradient. The available experimental data on bodies of revolution is restricted to cones which have a zero pressure gradient and to bodies which have a varying pressure gradient. A scale model has been constructed and the experimental pressure distribution checked with theory.

SYMBOLS

C_p pressure coefficient

I image

$l = \dfrac{\sin \mu \tan \mu \sin \theta}{\cos(\theta + \mu)}$

L length of body

L_1 distance from nose to point of r_{max}

$m = \dfrac{\sin \mu \tan \mu \sin \theta}{\cos(\theta - \mu)}$

M Mach number

O object

p static pressure

p_o stagnation pressure

p_o' stagnation pressure behind bow shock

$q = \dfrac{\gamma}{2} pM_\infty^2$

r radius

R Reynolds number

V velocity

V_l limiting velocity

W limiting velocity ratio, V/V_l

x,y coordinates of flow field

$\alpha = \dfrac{\theta_c + \theta_a}{2}$

$\beta = \epsilon - \delta$

$\delta = \theta_g + d\theta_{g,h}$

ϵ shock angle

γ ratio of specific heats, 1.405

$\lambda_I = \frac{dy}{dx} = \tan(\theta + \mu)$

$\lambda_{II} = \frac{dy}{dx} = \tan(\theta - \mu)$

η conical flow angle

θ stream direction

ϕ meridian angle about axis of symmetry

μ Mach angle

Subscripts:

b body

c cone

m mean value; when preceded by a 2, a second mean value is indicated

max maximum

n any point

N normal to shock

t theory

∞ free-stream conditions

a,b,c, . . . points in the characteristic net

METHOD OF DESIGN

A sharp-nose body of revolution with a prescribed pressure gradient may be designed in the following way: The nose can be considered conical for a short distance, and the values of the flow properties - μ the Mach angle and θ the stream direction - along the characteristic line af

(see fig. 1) can be determined for any conical flow angle η from reference 1. If C_p is assumed to be linear with x (see fig. 2), the slope of the body at any point is determined by the method of characteristics as outlined in reference 2. For a characteristic of λ_{II} (the entropy terms being disregarded), the basic formulas are as follows:

$$\frac{dy}{dx} = \tan(\theta - \mu) \tag{1}$$

$$\frac{dV}{V} + d\theta \tan \mu - m \frac{dx}{y} = 0 \tag{2}$$

If the limiting velocity ratio

$$\frac{V_l^{\,2}}{V^2} = \frac{1}{W^2} = 1 + \frac{2}{\gamma - 1} \frac{1}{M^2} \tag{3}$$

is introduced and equations (1) and (2) are applied to the determination of the flow properties at a point c on a specific body (figs. 1 and 2) with the following relations:

$$\begin{aligned} dW &= W_c - W_b \\ d\theta_{b,c} &= \theta_c - \theta_b \\ dx_{b,c} &= x_c - x_b \end{aligned} \tag{4}$$

where θ is measured in radians and equation (2) becomes

$$d\theta_{b,c} = \frac{\dfrac{m_b \, dx_{b,c}}{y_b} - \dfrac{W_c - W_b}{W_b}}{\tan \mu_b} \tag{5}$$

where

$$m = \left[\frac{\sin \theta \sin \mu \tan \mu}{\cos(\theta - \mu)}\right]_b \tag{6}$$

the θ_c corresponding to each value of $d\theta_{b,c}$ is

$$\theta_c = d\theta_{b,c} + \theta_b \tag{7}$$

The value of $dx_{b,c}$ and W_c to be used in equation (5) is determined as follows: Draw a straight line from point a to an intersection of the λ_{II} characteristic originating at point b. For an approximation, the angle of the line to the horizontal is slightly less than the slope of the conical surface leading to point a. This intersection is bracketed by several values of $dx_{b,c}$ and their corresponding values of W_c are determined from the C_p variation given in figure 2 and the following relations:

$$\left(\frac{p}{p_o'}\right)_n = \left(\frac{p}{p_o}\right)_n \frac{p_o}{p_o'} = \left[C_{p_n} \frac{\gamma}{2} \left(\frac{p}{p_o}\right)_\infty M_\infty^2 + \left(\frac{p}{p_o}\right)_\infty\right] \frac{p_o}{p_o'} \tag{8}$$

$$\frac{p_o'}{p_o} = \left[\frac{(\gamma + 1)M_N^2}{(\gamma - 1)M_N^2 + 2}\right]^{\frac{\gamma}{\gamma-1}} \left[\frac{\gamma + 1}{2\gamma M_N^2 - (\gamma - 1)}\right]^{\frac{1}{\gamma-1}} \tag{9}$$

$$M_N = M_\infty \sin \epsilon \tag{10}$$

The variation of p_o'/p_o with the curved portion of the shock will be disregarded and the ratio taken as that due to the initial cone. In order to determine the Mach number at any point n on the surface, the following equation is used:

$$M_n = \sqrt{\frac{2}{\gamma - 1}\left[\left(\frac{p_o'}{p_n}\right)^{\frac{\gamma-1}{\gamma}} - 1\right]} \tag{11}$$

If equation (3) is used, W_n can be determined and

$$\mu_n = \sin^{-1}\sqrt{\left(\frac{1}{W_n^2} - 1\right)\frac{\gamma - 1}{2}} \tag{12}$$

A second condition must be satisfied for the final evaluation of the properties of point c. A geometric relation for x_c and θ_c is obtained by writing the equations for the lines ac and bc; thus,

$$x_c = \frac{x_b \tan(\theta - \mu)_b - x_a \tan \alpha + y_a - y_b}{\tan(\theta - \mu)_b - \tan \alpha} \tag{13}$$

where

$$\alpha = \frac{\theta_c + \theta_a}{2} \tag{14}$$

Equation (13) is solved for several values of $\alpha \leqq \theta$ at the preceding point on the body. The results of equations (13) and (5) are plotted against $dx_{a,c}$ where

$$dx_{a,c} = x_c - x_a \tag{15}$$

The intersection of the two curves represents the point c. The terms μ_c and M_c are obtained by substituting the intersection values into equations (11) and (12).

In order to obtain a second approximation of the properties of the flow at a point on the body, equations (6) and (7) are written:

$$\theta_{c,m} = \frac{\dfrac{m_{b,m}\, dx_{b,c}}{\dfrac{y_b + y_c}{2}} - \dfrac{W_c - W_b}{\dfrac{W_b + W_c}{2}}}{\tan \dfrac{\mu_b + \mu_c}{2}} + \theta_b \tag{16}$$

$$m_{b,m} = \frac{\sin \dfrac{\theta_b + \theta_c}{2} \sin \dfrac{\mu_b + \mu_c}{2} \tan \dfrac{\mu_b + \mu_c}{2}}{\cos\left(\dfrac{\theta_b + \theta_c}{2} - \dfrac{\mu_b + \mu_c}{2}\right)} \tag{17}$$

where the subscript c refers to the intersection values of the first approximation. Equation (13) is rewritten as

$$x_{c,m} = \frac{x_b \tan\left(\dfrac{\theta_b + \theta_c}{2} - \dfrac{\mu_b + \mu_c}{2}\right) + y_a - y_b - x_a \tan \alpha_m}{\tan\left(\dfrac{\theta_b + \theta_c}{2} - \dfrac{\mu_b + \mu_c}{2}\right) - \tan \alpha_m} \tag{18}$$

Equation (14) becomes

$$\theta_{c,m} = 2\alpha_m - \theta_a \tag{19}$$

The results of equations (18) and (16) are plotted as $\theta_{c,m}$ against $dx_{a,c,m}$ and from this plot the intersection values are determined. For a body with a negative pressure gradient, the slope at any point on the surface must have $\theta_n \leqq \theta_{n-1}$.

The equations for determining the flow properties of a field point and a point on the curved portion of the bow shock by the method of characteristics have been presented in the literature and are presented for the convenience of the reader in appendix A.

The finite distances between the computed points along the surface of the body are determined by the number of η (fig. 1) used between η_c and $\eta = \epsilon$ on the conical nose. On the afterportion of the body, the characteristics are widely separated, the slope of the surface is changing rapidly, and no intersection of the characteristic with the surface of the body is obtained behind point t. (See fig. 3(a).) A new field point u corresponding to a more closely spaced characteristic net (see fig. 3(a)) is obtained by averaging all the properties of the points t and r. A more detailed characteristic net used to determine the afterportion of the body is presented in figure 3(b).

The number of approximations necessary to insure a high degree of accuracy was determined by applying the method of this report to a body of revolution with zero pressure gradient (a cone) with $\eta_c = 15^\circ$ and $M_\infty = 3.02$. The points a, b, d, and so forth, of figure 1 were determined from reference 1. The computed θ (along the surface) rapidly approaches its true value asymptotically; that is, a first approximation of the point c gave $\theta_c = 14.82^\circ$; a second approximation, $\theta_{c,m} = 14.99^\circ$; and a third approximation, $\theta_{c,2m} = 14.993^\circ$. A second body point was computed by using the second-approximation values of points c and e. The results were $\theta_l = 14.80^\circ$ and $\theta_{l,m} = 14.97^\circ$.

The pressure distribution of a parabolic body used in reference 3 was determined by the method of characteristics. The resulting pressure distribution was used to determine several ordinates and slopes on the initial portion of the nose of the body by the method outlined in this report which used the second-approximation values. A comparison of the resultant body with the original body is presented in table I and indicates close agreement.

APPLICATION OF THE METHOD TO THE DESIGN OF A SPECIFIC BODY

Design Specifications and Attainment

In order to obtain experimental corroboration of the method outlined in this report, a model with the following conditions was designed: $M_\infty = 3.13$, $\frac{dC_p}{d(x/L)} = 0.3202$, and $\eta_c = 15^\circ$ with an initial cone length of 1 inch. The x/L, y/L, θ, M, and C_p for the resultant body are shown in figure 4.

The downstream end of the body is defined by the method of characteristics as the point on the contour where the local static pressure becomes zero and can be determined from the following relation for a constant $\frac{dC_p}{d(x/L)}$:

$$L = \frac{x_a}{\frac{\Delta p}{q\,\frac{dC_p}{d(x/L)}} + 1} \tag{20}$$

where x_a is the ordinate corresponding to the base of the conical nose and

$$\Delta p = p_{x=a} - p_{x=L} = p_{x=a} \tag{21}$$

The description of the flow by the characteristic net in the vicinity of this limiting length is extremely laborious and from the nature of the flow has no physical significance. Accordingly, the net was terminated at $\frac{x}{L} = 0.9895$ (which will be designated L_b) where $M = 6.203$. The maximum radius of the body $\left(\frac{r}{L_b} = 0.1016\right)$ occurred at $\frac{x}{L_b} = 0.6678$ and the resultant fineness ratio was 4.919.

The Bell Telephone Laboratories X-66744 relay computer at the Langley Laboratory was used for the computations of the example body up to 88.8 percent of L. The averaging process previously described for determining a more closely spaced characteristic net had to be computed on desk calculators. This method is very time consuming and requires 605 hours for the computation of the entire body (425 hours on the Bell machine and 180 hours on the desk calculators). As a comparison,

the average time for computing the pressure distribution for a body of revolution with a given contour by the method of characteristics on the Bell machine is 120 hours. Convergence on a solution could be expedited with a different machine from those available for the computation of this project.

Computation of C_p for Off-Design Mach Number Operation

In order to determine the effect of varying the free-stream Mach number on the body which had a linear pressure distribution at $M_\infty = 3.13$, the pressure distribution was computed by the method of characteristics for $M_\infty = 3.02$ and $M_\infty = 4.16$. The ordinates of the body are presented in table II.

The computations for $M_\infty = 3.02$ were terminated at the point where further computations would have to be done on desk calculators. The resultant surface Mach number and pressure coefficient are shown in figures 5 and 6, respectively. The plot of C_p against x/L indicates that the pressure distribution is almost linear for $M_\infty = 3.02$ but not for $M_\infty = 4.16$. A plot of dC_p/dx against x/L (fig. 7) is indicative of the effect of varying the free-stream Mach numbers.

Comparison of Constant-Pressure-Gradient Body With NACA RM-10 Research Missile

In order to illustrate the effect of body shape on the pressure distribution, the constant-pressure-gradient model is compared with the NACA RM-10 research missile. The contour of the NACA RM-10 model is defined as

$$r = \frac{x}{7.5}\left(1.0 - \frac{x}{L}\right)$$

where $L = 93$ inches for comparison with the constant-pressure-gradient model. The Mach number and the pressure distribution determined by the method of characteristics for the NACA RM-10 research missile at $M_\infty = 3.12$ are shown in figure 8. In figure 9, the slopes of the contours for the two bodies are shown where the abscissa is x/L_1 and L_1 is the distance from the nose to the point of r_{max}. The condition of constant pressure gradient requires a relatively blunt afterbody. It is obvious that the relation of constant pressure gradient implies an invariant relation of θ with x, and within reasonable limits the value of dp/dx is inversely proportional to the length.

APPARATUS AND TESTS

Tests on a model of the constant-pressure-gradient body were conducted in one of the blowdown jets of the Langley Gas Dynamics Branch. The test facility consisted of nozzle blocks to give $M = 3.05$ and $M = 3.13$ with test-section sizes of 8 by 10 inches and 9 by 9 inches, respectively. The test section of each set of nozzle blocks was calibrated by measuring the free-stream static pressure in the vertical center plane with the multitube rake shown in figure 10. High-pressure air was heated and discharged through the two-dimensional symmetrical nozzle and diffuser to the atmosphere. The pressures were measured on a mercury manometer board and photographically recorded. The results shown in figures 11 and 12 indicate that $M = 3.05 \pm 0.043$ and $M = 3.13 \pm 0.049$, respectively, over the entire region that was surveyed. A schlieren photograph of the flow in a region of the test section of the $M = 3.05$ nozzle at a Reynolds number per inch of 2.77×10^6 is shown in figure 13 and a schlieren of the flow in the $M = 3.13$ nozzle at a Reynolds number per inch of 2.64×10^6, in figure 14.

Measurement of aerodynamic characteristics that are affected by the boundary-layer development are governed by the transitional Reynolds number. The transitional Reynolds number was obtained by heat-transfer measurements on a 10° cone to indicate the steadiness of the free stream in this facility as compared with that of other NACA facilities. The method and results are discussed in appendix B.

The constant-pressure-gradient model has a length of 17.55 inches $\left(\frac{x}{L} = 0.9781\right)$ and a maximum diameter of 3.608 inches and is constructed of Paraplex with a steel central core and coated with heat-resistant phenolic lacquer for added strength and heat resistance. A sketch of the model and a table of ordinates are shown in figure 15 and a photograph of the model in figure 16. The completed model was accurately measured on a jig-boring machine and the resultant ordinates are plotted as a deviation of slope of the surface from the slope of the prescribed ordinates in figure 17. The differences between the prescribed and measured slopes are shown to be small. The model was mounted on a sting which was supported by a strut spanning the tunnel downstream of the diffuser. A sketch of the model and sting support mounted in the $M = 3.13$ tunnel is shown in figure 18. Thirty-five static-pressure orifices (0.020-inch inside diameter) were located at $\frac{1}{2}$-inch increments along a longitudinal element of the body with one orifice diametrically opposite the foremost orifice to determine the angle of attack. The pressures were measured on a multitube mercury manometer board and photographically recorded.

The effect of orifice size on the static-pressure measurements on a body of revolution with a small boundary layer was determined on a small 30° cone. Three orifices (0.004-, 0.0135-, and 0.0200-inch inside diameter, including the orifice size for the design model) were located at two axial stations corresponding to the locations of the first two static-pressure orifices on the constant-pressure-gradient model. A sketch of the model illustrating the size and location of the orifices is shown in figure 19 and a photograph of the model, in figure 20. The cone was tested with the orifices at $\phi = 0^{\circ}$ and 90° at $M_{\infty} = 3.13$ over the same range of free-stream Reynolds numbers used for the tests of the design model. A comparison of the measured Mach number with the predicted Mach number (ref. 1) indicated that the error is a maximum for the smallest orifice and is essentially zero for the orifice with a 0.020-inch inside diameter.

The effect of free-stream static-pressure variations on the longitudinal-pressure distribution for the design model was determined by rotating the model about its axis of symmetry and recording the pressures for $\phi = 0^{\circ}$, 90°, and 180°. In the $M = 3.05$ tunnel, the model was also tested at the three axial stations shown in figure 11 with the orifices at $\phi = 0^{\circ}$ to determine further the effect of flow discontinuities. The ranges of test Reynolds numbers based on body length were 3.61×10^{7} to 4.86×10^{7} for $M = 3.05$ and 3.76×10^{7} to 4.62×10^{7} for $M = 3.13$. Composite schlieren photographs taken during the tests are shown in figures 21 and 22.

ACCURACY OF TEST DATA

A number of pressures were measured for the purpose of determining the free-stream Mach number and the pressure coefficient along the model. The overall accuracy is dependent upon the individual accuracy of each measurement. The accuracy of measuring the stagnation pressure on a gage was ± 0.1 lb/in.^{2}, and the accuracy of reading it on a manometer board was ± 0.1 inch of mercury. The overall accuracy for determining C_p is ± 0.003. A comparison of the experimental points with the computed curve indicates a deviation greater than the accuracy of measuring C_p. This deviation is explained by the deviation of actual model contour from the design (see fig. 17) and the growth of boundary layer.

RESULTS AND DISCUSSION

Tests at $M = 3.05$

The schlieren photograph (fig. 13) shows several compression waves symmetrical about the horizontal center plane of the tunnel. The nozzle

calibration indicates that only one set of these waves has sufficient strength to be of concern. The model was tested in three axial positions (fig. 11) and three radial positions with the model in position 1. The results of these tests are plotted as C_p against x/L in figure 23 where the solid line is the computed distribution for $M_\infty = 3.02$. The region of compression causes a pressure rise at $\frac{x}{L} = 0.195$ to 0.31 with the model in position 1 and is moved forward to $\frac{x}{L} = 0.085$ to 0.20 with the model in position 2 in the tunnel. (These bumps are dotted for clarity of fig. 23(a).) In axial position 3 the compression does not intersect the body. The result of rotating the body about its axis of symmetry in position 1 is shown in figure 23(b). The pressure rise that occurs when the line of orifices intersect the compression wave is dotted for clarity. The slope of the compression can be determined from the schlieren (fig. 13) and can be checked with the results of rotating the model about its axis. The Reynolds number was varied from 36.1×10^6 to 48.6×10^6 with the model in position 1 and the orifice at $\phi = 0^\circ$. There was no effect on the pressure distribution (fig. 23(c)).

The experimental data (fig. 23) were corrected for the free-stream static-pressure variation by simple superposition except in the region of the bump. The bump in the C_p curve due to the compression waves in the nozzle was corrected by decreasing the measured static pressure by the ratio of the pressure rise across an oblique shock, the intensity of which corresponds to the decrease in Mach number shown in figure 11. The coarseness of the nozzle calibration allows considerable latitude in the detail of the Mach number distribution in the compression region and the distribution was assumed so that it was compatible with the calibration and eliminated the bump in the C_p curve. The effect of this compression had been completely eliminated when the compression distribution in the flow was applied as a correction to the model in all positions, as is shown in figure 24. An inspection of figure 24 shows an excellent agreement between the computed and experimental C_p curves.

The pressure rise in the vicinity of the base of the body is associated with the boundary-layer separation as seen in figure 21.

Tests at $M = 3.13$

The body was rotated about its axis of symmetry to evaluate the effect of the free-stream discontinuities on the longitudinal-pressure distribution. The experimental data corrected for the free-stream static-pressure variations by simple superposition are shown in figure 25(a) with the computed pressure distribution. The first two orifices located diametrically opposite from each other, 0.5 inch from the nose, have a

reversal of pressure differential for $\phi = 0^{\circ}$ and 180°; this reversal indicates that the model was at a slight angle of attack with the line of orifices on the windward side for $\phi = 0^{\circ}$. The Reynolds number was varied from 37.6×10^6 to 46.2×10^6 with the orifices at $\phi = 0^{\circ}$ with no effect on the pressure distribution (fig. 25(b)).

A close examination of the flow schlieren (fig. 22) shows the conical shock angle is greater than the computed value from reference 1, but the accuracy of measurement is not sufficient to determine the free-stream Mach number. A comparison of the boundary-layer thickness along the nozzle surface with that in figure 14 shows the boundary layer is approximately 0.032 inch thicker when the model is mounted in the tunnel. The effect of the model in the small test section might be to reduce the free-stream Mach number from 3.13 to 3.07. When $M = 3.07$ is used to reduce the experimental data, there is good agreement with the computed pressure distribution for the design conditions. The pressure rise in the vicinity of the base of the body is due to the boundary-layer separation.

CONCLUDING REMARKS

A method based upon the theory of characteristics has been developed to compute the contour of a body for a prescribed pressure distribution. An indication of the accuracy of the method was obtained by using the pressure distribution which had been determined by the conventional method of characteristics to compute the ordinates near the nose of a body. The agreement between the original and calculated ordinates was good. The contour of a body with a constant pressure gradient at a Mach number of 3.13 was computed; a model was constructed and tested at Mach numbers of 3.05 and 3.13. Excellent agreement with the computed distribution was obtained.

Langley Aeronautical Laboratory,
National Advisory Committee for Aeronautics,
Langley Field, Va., October 21, 1955.

APPENDIX A

EQUATION FOR DETERMINING THE FLOW PROPERTIES OF A FIELD POINT

The equations for determining the flow properties of a field point and a point on the curved portion of the bow shock have been given in many references and are presented in this appendix for the convenience of the reader.

The equations for the first approximation of a field point e (fig. 1) are as follows:

$$x_e = \frac{y_c - y_d - x_c \tan(\theta_c + \mu_c) + x_d \tan(\theta_d - \mu_d)}{\tan(\theta_d - \mu_d) - \tan(\theta_c + \mu_c)} \tag{A1}$$

$$y_e = (x_e - x_d)\tan(\theta_d - \mu_d) + y_d \tag{A2}$$

$$\theta_e = \theta_c + \frac{1 - \frac{W_c}{W_d} - (\theta_c - \theta_d)\tan \mu_d + \frac{m_d}{y_d}(x_e - x_d) - \frac{l_c}{y_c}(x_e - x_c)\frac{W_c}{W_d}}{\frac{W_c}{W_d}\tan \mu_c + \tan \mu_d} \tag{A3}$$

where

$$l_c = \frac{\sin \mu \tan \mu \sin \theta}{\cos(\theta + \mu)} \tag{A4}$$

Then,

$$W_e = W_c + W_c\left[(\theta_e - \theta_c)\tan \mu_c + \frac{l_c}{y_c}(x_e - x_c)\right] \tag{A5}$$

The term μ_e is determined from equation (12).

The equations for the second approximation are as follows:

$$x_{e,m} = \frac{y_c - y_d + x_d \tan\left(\frac{\theta_d + \theta_e}{2} - \frac{\mu_d + \mu_e}{2}\right) - x_c \tan\left(\frac{\theta_c + \theta_e}{2} + \frac{\mu_c + \mu_e}{2}\right)}{\tan\left(\frac{\theta_d + \theta_e}{2} - \frac{\mu_d + \mu_e}{2}\right) - \tan\left(\frac{\theta_c + \theta_e}{2} + \frac{\mu_c + \mu_e}{2}\right)} \tag{A6}$$

$$y_{e,m} = \left(x_{e,m} - x_d\right)\tan\left(\frac{\theta_d + \theta_e}{2} - \frac{\mu_d + \mu_e}{2}\right) + y_d \tag{A7}$$

$$d\theta_{c,e,m} = \frac{\dfrac{\dfrac{W_d - W_c}{W_d + W_e}}{2} - \left(\theta_c - \theta_d\right)\tan\dfrac{\mu_d + \mu_e}{2} + \left(x_{e,m} - x_d\right)\dfrac{m_{d,m}}{\dfrac{y_d + y_e}{2}} - \dfrac{2\left(W_c + W_e\right)}{W_d + W_e}\, l_{c,m}\,\dfrac{x_{e,m} - x_c}{y_c + y_e}}{\tan\dfrac{\mu_d + \mu_e}{2} + \dfrac{W_c + W_e}{W_d + W_e}\tan\dfrac{\mu_c + \mu_e}{2}} \tag{A8}$$

$$l_{c,m} = \frac{\sin\dfrac{\mu_c + \mu_e}{2}\tan\dfrac{\mu_c + \mu_e}{2}\sin\dfrac{\theta_c + \theta_e}{2}}{\cos\left(\dfrac{\theta_c + \theta_e}{2} + \dfrac{\mu_c + \mu_e}{2}\right)} \tag{A9}$$

$$\theta_{e,m} = d\theta_{c,e,m} + \theta_c \tag{A10}$$

$$W_{e,m} = \left[\left(\theta_{e,m} - \theta_c\right)\tan\frac{\mu_c + \mu_e}{2} + l_{c,m}\frac{x_{e,m} - x_c}{\dfrac{y_c + y_e}{2}}\right]\frac{W_c + W_e}{2} + W_c \tag{A11}$$

The final x-value of the field point is that calculated from equation (A6) where $x_{e,m}$ corresponds to an average value of μ and θ for the first approximation obtained by using points c, d, and e.

In order to determine the properties of point h, the intersection of a λ_I characteristic with the bow shock, assume the line fh (fig. 1) is a straight line, the slope of which is $\tan \epsilon$, and the line gh is straight with a slope of $\tan(\mu + \theta)_g$. As a result,

$$x_h = \frac{y_g - y_f + x_f \tan \epsilon - x_g \tan(\mu + \theta)_g}{\tan \epsilon - \tan(\mu + \theta)_g} \tag{A12}$$

and

$$y_h = (x_h - x_f)\tan \epsilon + y_f \tag{A13}$$

With the use of the general equation of a shock,

$$\frac{W_{\theta,g}}{W_g} - 1 + \left(\frac{dW}{d\delta}\right)_{\theta_g} \frac{d\theta_{g,h}}{W_g} - d\theta_{g,h} \tan \mu_g - \frac{x_h - x_g}{y_g} l_g = 0 \tag{A14}$$

Then

$$d\theta_{g,h} = \frac{\frac{x_h - x_g}{y_g} l_g + 1 - \frac{W_{\theta,g}}{W_g}}{\left(\frac{dW}{d\delta}\right)_{\theta_g} \frac{1}{W_g} - \tan \mu_g} \tag{A15}$$

where the subscript θ_g corresponds to a deviation across the shock at h equal to θ of point g. Therefore,

$$\theta_h = \delta_h = \theta_g + d\theta_{g,h} \tag{A16}$$

and

$$W_h = W_{\theta,g} + \left(\frac{dW}{d\delta}\right)_{\theta_g} d\theta_{g,h} \tag{A17}$$

The method of determining $(dW/d\delta)_{\theta_g}$ and $W_{\theta,g}$ will be presented after the equations for the second approximation of point h which are as follows:

$$x_{h,m} = \frac{y_g - y_f + x_f \tan \frac{\epsilon + \epsilon_h}{2} - x_g \tan \frac{\mu_g + \theta_g + \mu_h + \theta_h}{2}}{\tan \frac{\epsilon + \epsilon_h}{2} - \tan \frac{\mu_g + \theta_g + \mu_h + \theta_h}{2}} \tag{A18}$$

$$d\theta_{g,h,m} = \frac{\dfrac{x_{h,m} - x_g}{y_{g,m}} l_{g,m} + \dfrac{W_g - W_{\theta,g}}{W_{g,m}}}{\left(\dfrac{dW}{d\delta}\right)_{\theta_g} \dfrac{1}{W_{g,m}} - \tan \mu_{g,m}} \tag{A19}$$

$$W_{h,m} = W_{\theta,g} + \left(\frac{dW}{d\delta}\right)_{\theta_g} d\theta_{g,h,m} \tag{A20}$$

$$\theta_{h,m} = \delta_{h,m} = \theta_g + d\theta_{g,h,m} \tag{A21}$$

The term $l_{g,m}$ is computed from equation (A9) by substituting g for c and h for e. The terms $\left(\frac{dW}{d\delta}\right)_{\theta_g}$ and $W_{\theta,g}$ are constant for both first and second approximations. The shock angle corresponding to $\delta_{h,m}$ is used to determine the next point on the shock but not to determine the location of point h_m.

As outlined in reference 2, $dW/d\delta$ is the tangent, at the point $\delta = \theta_g$, to the curve that represents W as a function of δ. The usual procedure is to determine this property graphically and regard the quantity as constant along the curved portion of the shock. An analytical expression is necessary to determine $dW/d\delta$ to a more accurate degree and to consider the curvature of the bow shock for computing the characteristic net on a Bell Laboratories X-66744 relay computer. If the two-dimensional shock equation is used,

$$\frac{1}{\tan \delta} = \left(\frac{\gamma + 1}{2} \frac{M_\infty^2}{M_\infty^2 \sin^2 \epsilon - 1} - 1\right) \tan \epsilon \tag{A22}$$

and

$$\frac{\tan \epsilon}{\tan \beta} = \frac{2}{\gamma + 1}\left(\frac{1}{M_2^2 \sin^2 \beta} + \frac{\gamma - 1}{2}\right) \tag{A23}$$

Since

$$\frac{d}{d\delta} \frac{1}{\tan \delta_A} = -\left(1 + \frac{1}{\tan^2 \delta_A}\right) \tag{A24}$$

then, by using the notation of this report,

$$\frac{d}{d\epsilon}\frac{1}{\tan\delta_g} = \left(\frac{\gamma + 1}{2}\frac{M_\infty{}^2}{M_\infty{}^2\sin^2\epsilon_g - 1} - 1\right)\frac{1}{\cos^2\epsilon_g} -$$

$$\frac{\gamma + 1}{2}\left(\frac{M_\infty{}^2}{M_\infty{}^2\sin^2\epsilon_g - 1}\right)^2 2\sin^2\epsilon_g \tag{A25}$$

$$\frac{d\epsilon}{d\delta_g} = \frac{\frac{d}{d\delta}\frac{1}{\tan\delta_g}}{\frac{d}{d\epsilon}\frac{1}{\tan\delta_g}} \tag{A26}$$

$$\frac{1}{M_{\theta,g}{}^2} = \sin^2(\epsilon_g - \delta_g)\left(\frac{\gamma + 1}{2}\frac{\tan\epsilon_g}{\tan(\epsilon_g - \delta_g)} - \frac{\gamma - 1}{2}\right) \tag{A27}$$

$$\frac{d}{d\delta}\left(\frac{1}{M_{\theta,g}{}^2}\right) = \frac{\gamma + 1}{2}\left\{\tan\epsilon_g\left(\frac{d\epsilon}{d\delta_g} - 1\right)\left[\cos^2(\epsilon_g - \delta_g) - \sin^2(\epsilon_g - \delta_g)\right] + \right.$$

$$\left.\sin(\epsilon_g - \delta_g)\cos(\epsilon_g - \delta_g)\frac{1}{\cos^2\epsilon_g}\frac{d\epsilon}{d\delta_g}\right\} -$$

$$\frac{\gamma - 1}{2}\left[2\sin(\epsilon_g - \delta_g)\cos(\epsilon_g - \delta_g)\left(\frac{d\epsilon}{d\delta_g} - 1\right)\right] \tag{A28}$$

$$\frac{1}{W_{\theta,g}{}^2} = 1 + \frac{2}{\gamma - 1}\frac{1}{M_{\theta,g}{}^2} \tag{A29}$$

$$\frac{dW}{d\left(\frac{1}{M_{\theta,g}{}^2}\right)} = -W_{\theta,g}{}^3\frac{1}{\gamma - 1} \tag{A30}$$

$$\frac{dW}{d\delta_g} = \frac{dW}{d\left(\frac{1}{M_{\theta,g}{}^2}\right)}\frac{d}{d\delta}\frac{1}{M_{\theta,g}{}^2} \tag{A31}$$

The variation of $dW/d\delta$ from the point where shock curvature begins to the last point on the shock where a characteristic of λ_{II} family intersects the stern of the body (see fig. 26) was computed for the constant-pressure-gradient model. For $M_\infty = 3.13$, $dW/d\delta$ varied from -0.33937 at v_1 to -0.31145 at v_{n+1}.

APPENDIX B

METHOD OF DETERMINING THE TRANSITIONAL REYNOLDS NUMBER OF THE $M = 3.13$ NOZZLE

In a project of this type, where a computed distribution is to be compared with the actual pressure distribution on a body of revolution, it is interesting to know the nature of the boundary layer because of its effect on the model contour.

The boundary-layer transition Reynolds number on a 10° cone has been used as a measure of the steadiness of the free stream in various NACA facilities (ref. 4). A similar highly polished thin-walled cone was used to determine the R_{tr} by surface-temperature measurements in the $M = 3.13$ jet. The high free-stream Reynolds number per foot produces an extremely thin boundary layer which requires that the ratio of average height of surface roughness to height of boundary layer be small. The ratio is made small by a high degree of polish on the model surface and by reducing the free-stream Reynolds number.

The model with a 0.050-inch skin thickness was machined from a single piece of stainless steel. The surface was successively ground with No. 1/0, No. 2/0, and No. 3/0 fine emery papers and the direction of grinding with each paper was alternated from circumferential to axial, and conversely. A cutting oil of 5 percent paraffin with filtered kerosene was used with each grinding. The final polish was obtained with a commercial polish which contains a chromium grit whose average size is 1 micron.

The temperature distribution along the surface of the model was determined by 18 iron-constantan thermocouples installed in a 20° helix about the conical body with the first thermocouple located 3/4 inch from the nose as shown in figure 27 and a picture of the completed model in figure 28. A continuous record of the surface-temperature variation was made throughout the test with a multi-channel recording oscillograph.

In order to facilitate a closer inspection of the boundary layer by visual means, a schlieren system similar to that in reference 5, which permits magnification greater in a plane normal to the flow than in the direction of the flow, was constructed. The system incorporates three spectacle-size lenses: one spherical and two cylindrical. The optical diagrams are shown in figure 29. A magnification of 6, normal to the flow, was obtained with this lens system incorporating a +34 diopter cylindrical lens with a horizontal axis (lens no. 4 in fig. 29) and a

+6 diopter cylinder with a vertical axis (lens no. 5 in fig. 29). The lens mount in figure 30 allows the lens position and cylinder axes to be varied. A comparison of the 10° cone using a conventional schlieren with this system is shown in figure 31. A 1-inch grid is superimposed on the asymmetrical schlieren. Since the lens system was not achromatic, a filter which transmits the yellow portion of the spectrum was used.

A second minimum was installed to reduce the stagnation pressure and thereby reduce the free-stream Reynolds number R_{∞} and move the transition point onto the instrumented portion of the cone and to a point where the boundary layer has a substantial thickness. The diffuser consisted of two 11° wedges with a length adjusted to avoid choking. The portion of the diffuser downstream of the second minimum was extended to a point beyond the model support as shown in figure 32. This extension allowed the stagnation pressure to be reduced from 160 lb/in.^{2} to 65 lb/in.^{2} gage and a corresponding reduction of Reynolds number per inch from 2.15×10^6 to 0.894×10^6.

The variation of the transitional Reynolds number with free-stream Reynolds number is shown in figure 33. The transition point corresponding to this curve is accurate to $\pm\frac{1}{4}$ inch.

The transition point was also determined from the flow schlieren (fig. 34) and the corresponding transitional Reynolds number is plotted in figure 33. The tests indicate that the transition point on the constant-pressure-gradient model is so far forward that the boundary layer is turbulent on the entire model.

REFERENCES

1. Staff of the Computing Section, Center of Analysis (Under Direction of Zdeněk Kopal): Tables of Supersonic Flow Around Cones. Tech. Rep. No. 1, M.I.T., 1947.

2. Ferri, Antonio: Elements of Aerodynamics of Supersonic Flows. The MacMillan Co., 1949.

3. Scherrer, Richard: Comparison of Theoretical and Experimental Heat-Transfer Characteristics of Bodies of Revolution at Supersonic Speeds. NACA Rep. 1055, 1951. (Supersedes NACA RM A8L28 by Scherrer, Wimbrow, and Gowen; NACA TN 1975 by Wimbrow; NACA TN 2087 by Scherrer and Gowen; NACA TN 2131 by Scherrer; and NACA TN 2148 by Wimbrow and Scherrer.)

4. Ross, Albert O.: Determination of Boundary-Layer Transition Reynolds Numbers by Surface-Temperature Measurements of a 10° Cone in Various NACA Supersonic Wind Tunnels. NACA TN 3020, 1953.

5. Buchele, Donald R., and Goossens, Herman R.: Lens System Producing Unequal Magnification in Two Mutually Perpendicular Directions. The Review of Scientific Instruments, vol. 25, no. 3, Mar. 1954, pp. 262-263.

TABLE I.- COMPARISON OF ORDINATES COMPUTED FROM THE KNOWN PRESSURE DISTRIBUTION WITH THE ACTUAL ORDINATES OF A PARABOLIC BODY AT $M_\infty = 3.02$

Method	x, in.	y, in.	θ, deg
Pressure	1.0354	0.33618	17.540
Computed[1]	1.0354	.33620	17.541
Pressure	1.0785	.34979	17.500
Computed[1]	1.0785	.34981	17.503
Pressure	1.1236	.36400	17.462
Computed[1]	1.1236	.36401	17.464

[1]Computed by the method of characteristics with contour of the body defined by the equation

$$\frac{y}{L} = \frac{1}{3}\left[\frac{x}{L} - \left(\frac{x}{L}\right)^2\right]$$

where $L = 40$.

TABLE II.- ORDINATES FOR THE CONSTANT-PRESSURE-GRADIENT MODEL

DETERMINED BY THE METHOD OF CHARACTERISTICS

x/L	r/L	x/L	r/L
0.013900	0.0037244	0.10012	0.025672
.014495	.0038838	.10896	.027797
.015120	.0040507	.11986	.030383
.015777	.0042262	.13383	.033645
.016472	.0044115	.14475	.036153
.017211	.0046081	.15204	.037806
.017999	.0048175	.15979	.039545
.018843	.0050419	.16805	.041379
.019754	.0052833	.17696	.043330
.020740	.0055447	.18659	.045408
.021815	.0058292	.19707	.047637
.022995	.0061412	.20858	.050041
.024301	.0064860	.22126	.052638
.025760	.0068703	.23542	.055471
.027405	.0073034	.25135	.058576
.029286	.0077975	.26949	.062000
.031470	.0083700	.29042	.065802
.034058	.0090465	.31500	.070058
.037204	.0098667	.34442	.074843
.041172	.010897	.38064	.080258
.042472	.011234	.42679	.086351
.044234	.011689	.48878	.093003
.046251	.012210	.57912	.099151
.048374	.012757	.61182	.10025
.050616	.013333	.66079	.10058
.053003	.013944	.72415	.098326
.055549	.014595	.80423	.090034
.058283	.015291	.85734	.080054
.061241	.016042	.88806	.072029
.064445	.016853	.92456	.059352
.067957	.017738	.95000	.047426
.071823	.018708	.96611	.037746
.076121	.019781	.97610	.030486
.080945	.020980	.98209	.025457
.086427	.022332	.98742	.020324
.092729	.023877	.98954	.018061

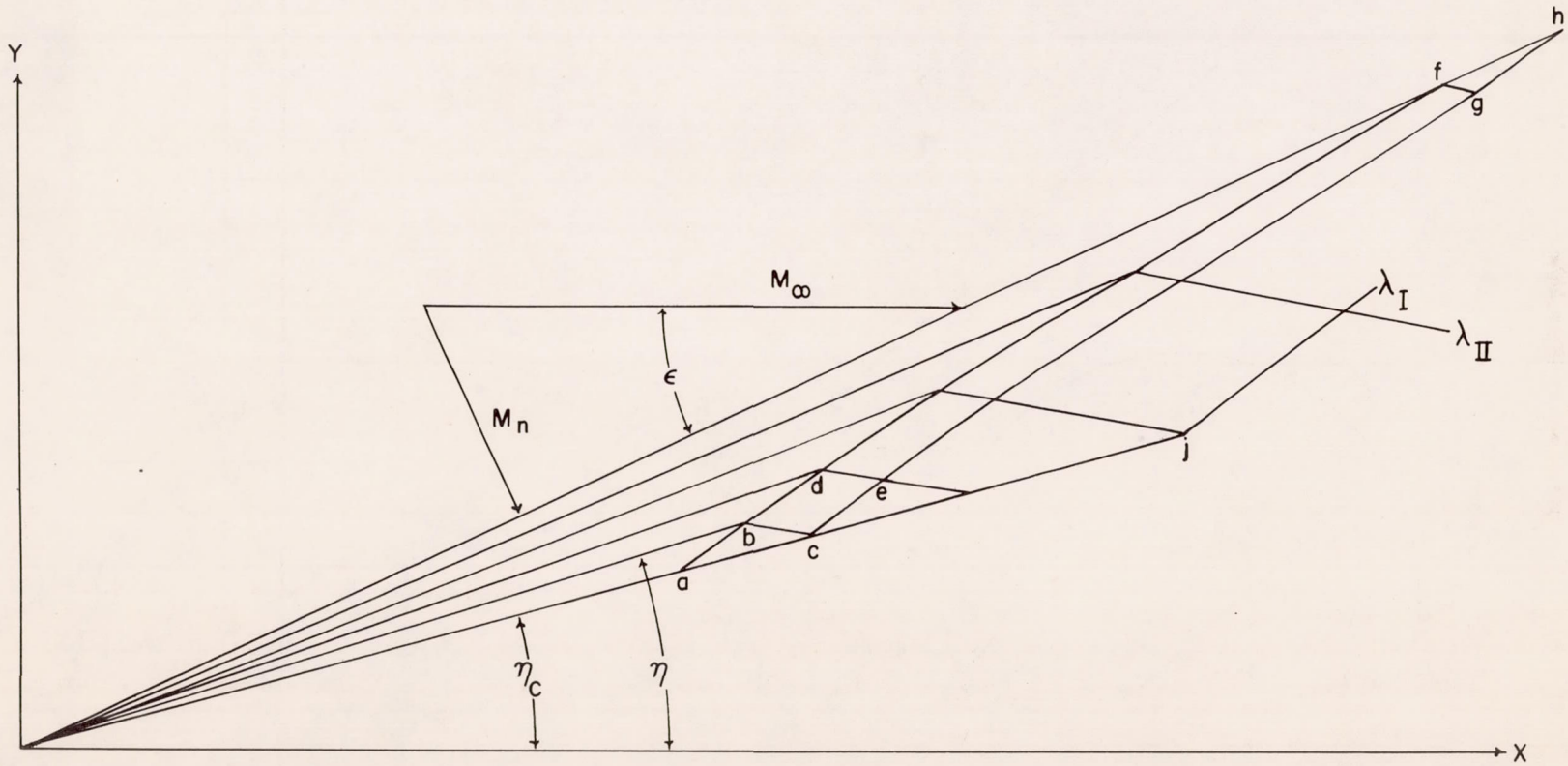

Figure 1.- Characteristic net for nose of body.

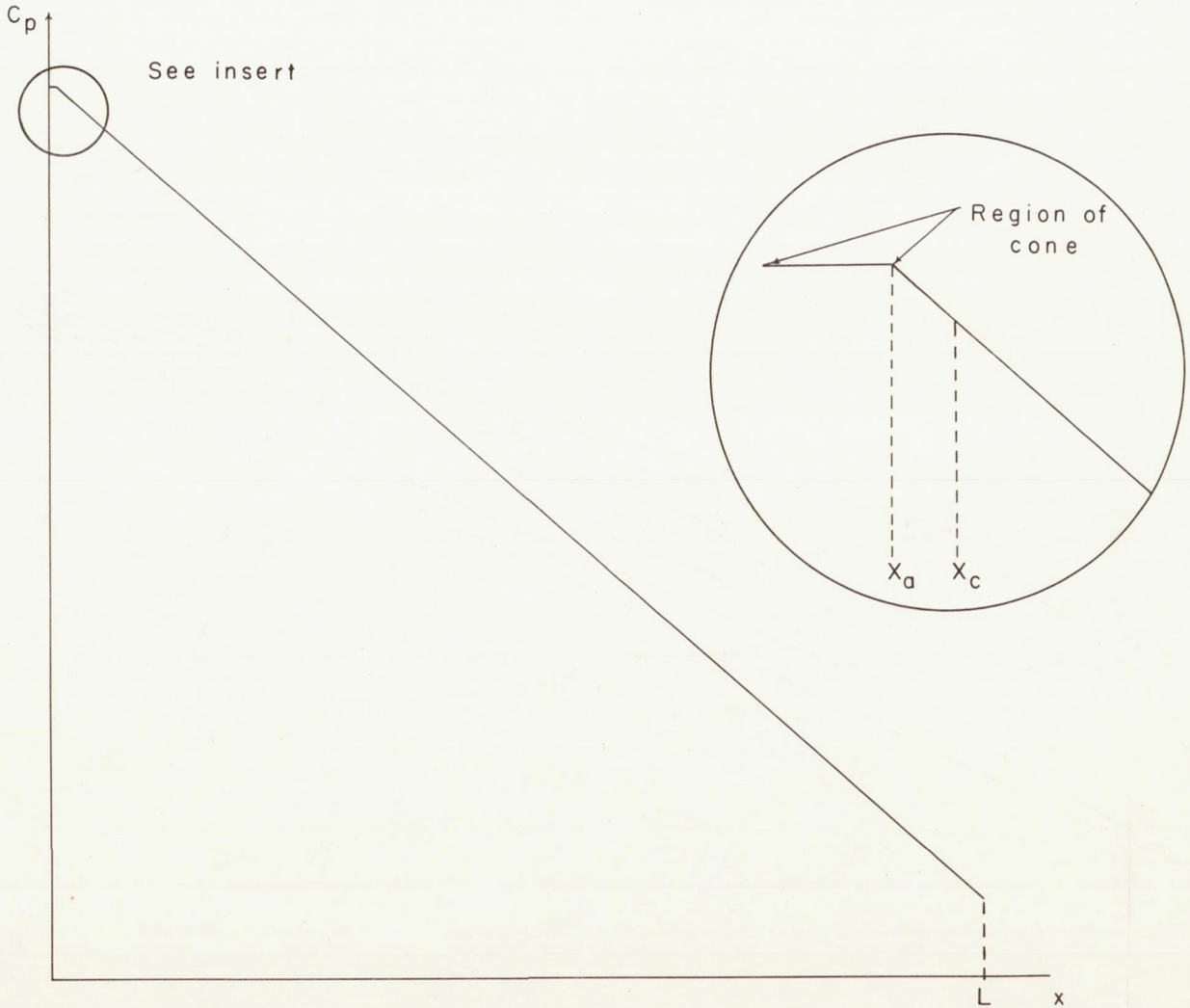

Figure 2.- Assumed axial variation of pressure coefficient for body of revolution.

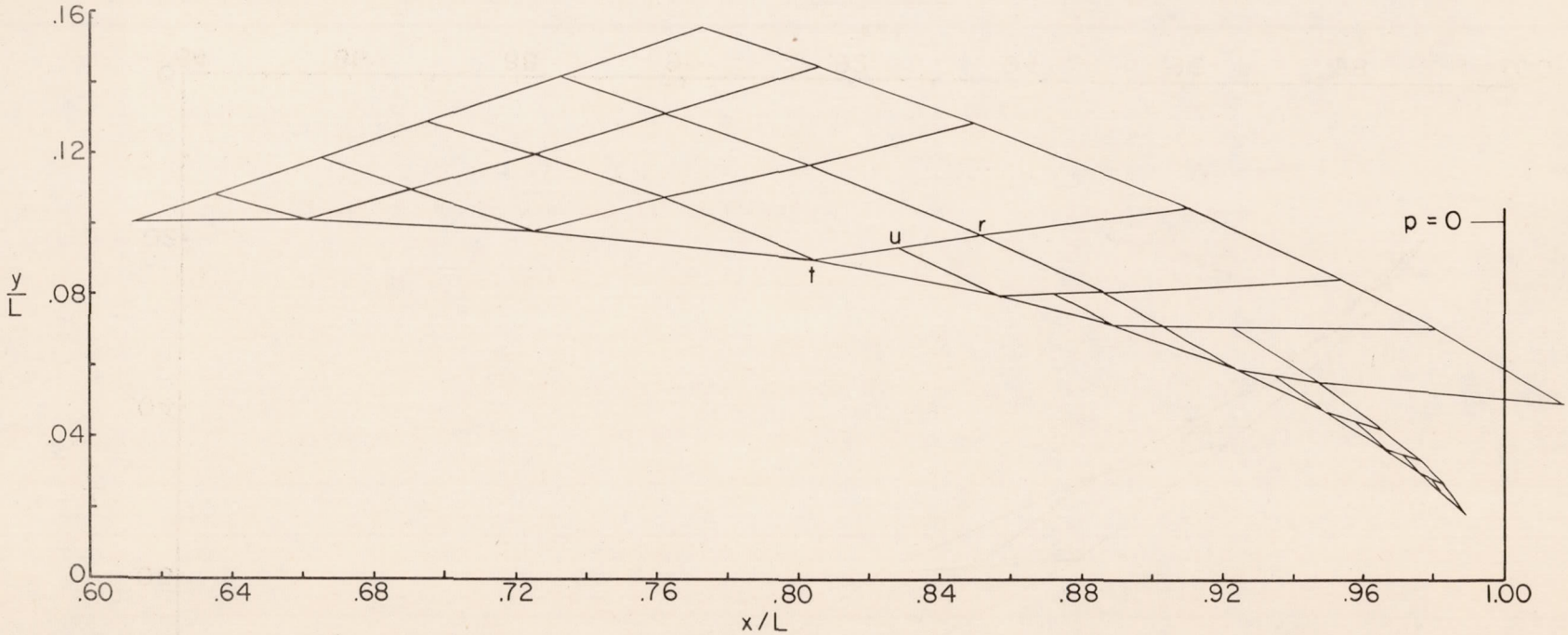

(a) Station 44 to 71.1.

Figure 3.- Characteristic net for afterportion of body.

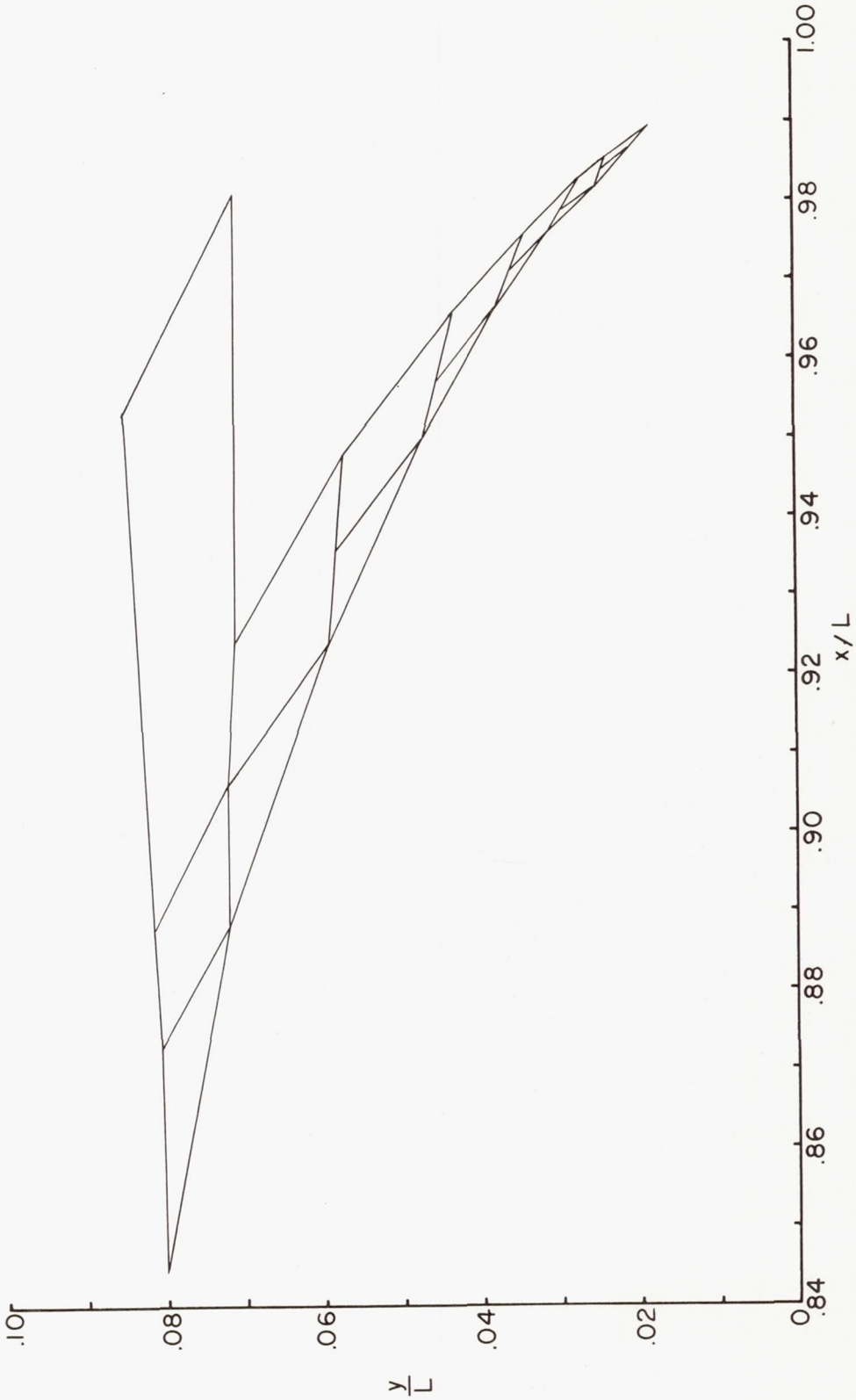

(b) Station 62 to 71.9.

Figure 3.- Concluded.

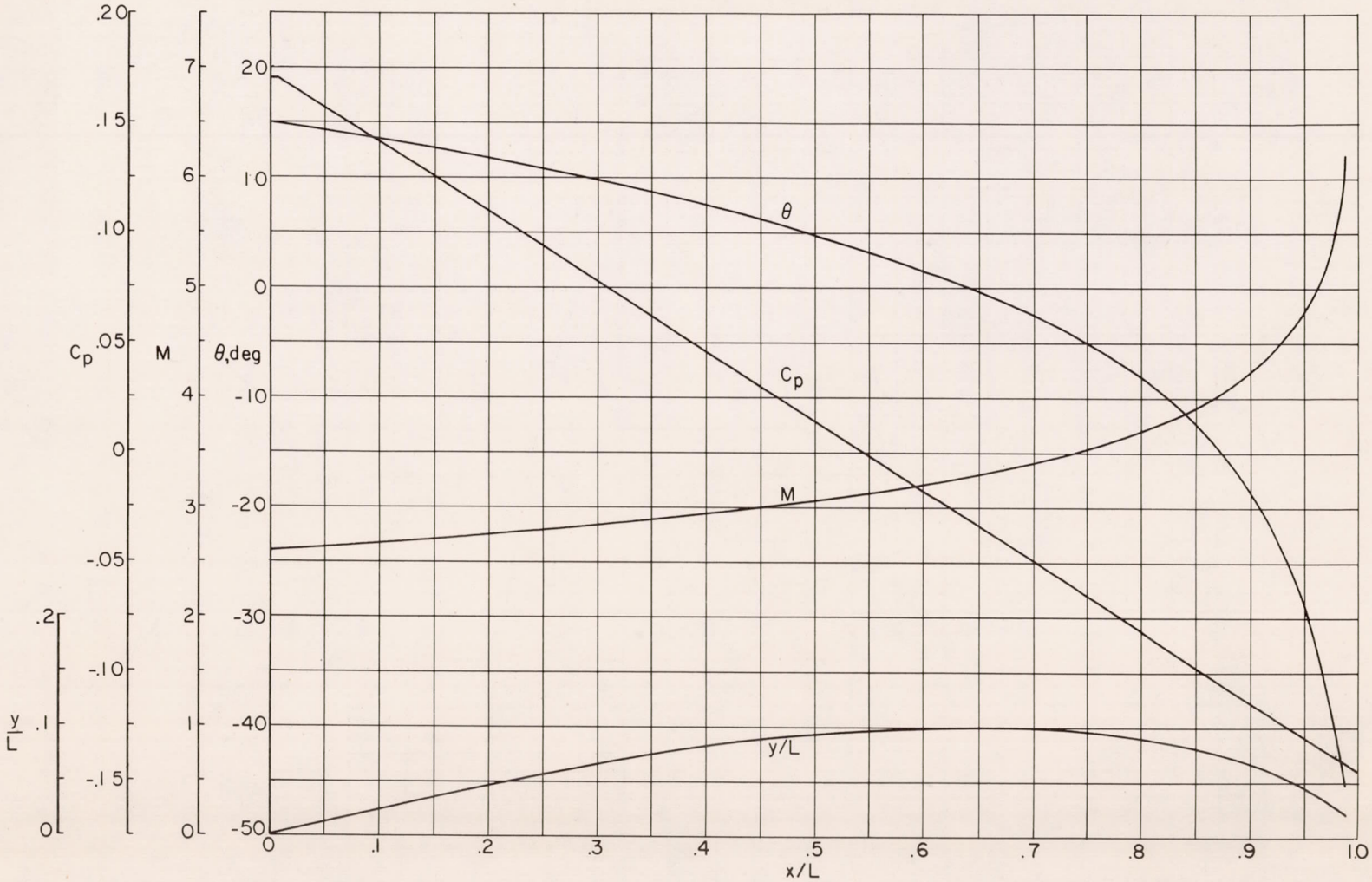

Figure 4.- Axial variation of M, C_p, y/L, and θ for constant-pressure-gradient body at $M_\infty = 3.13$.

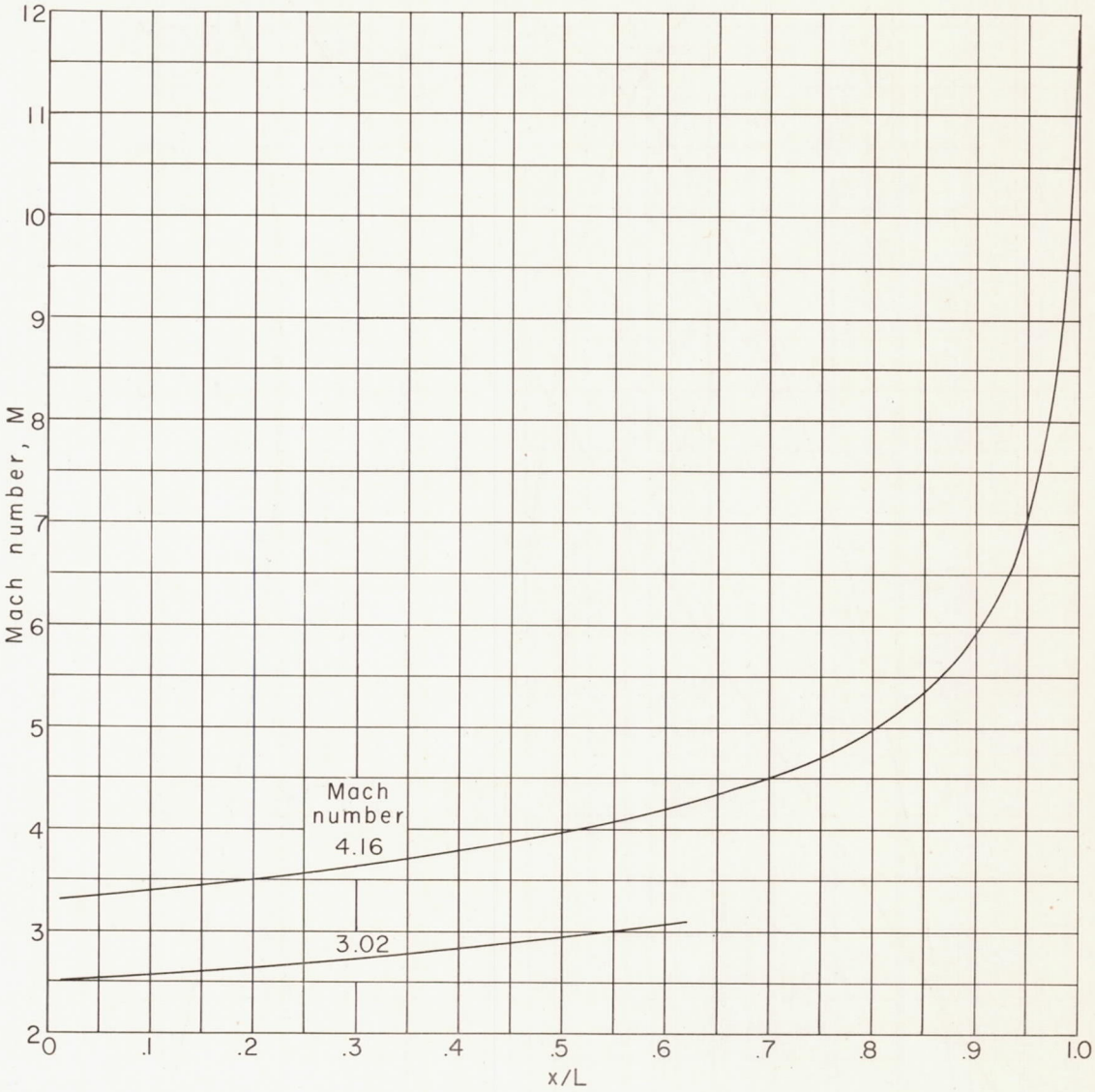

Figure 5.- Axial variation of surface Mach number for a body designed to have constant dp/dx at $M_\infty = 3.13$ when operating at $M_\infty = 3.02$ and $M_\infty = 4.16$.

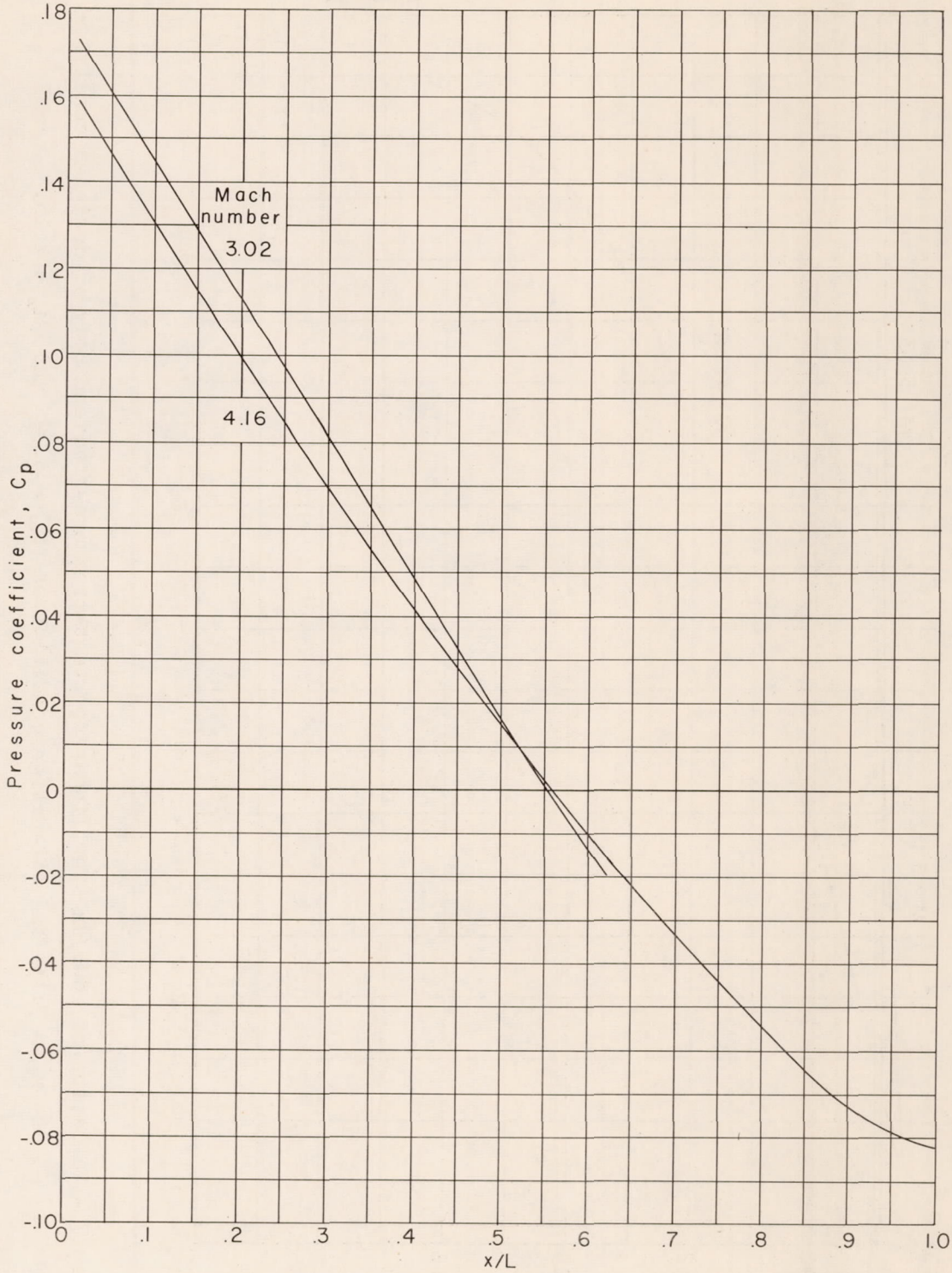

Figure 6.- Axial variation of pressure coefficient for body of figure 4 when operated at $M_\infty = 3.02$ and $M_\infty = 4.16$.

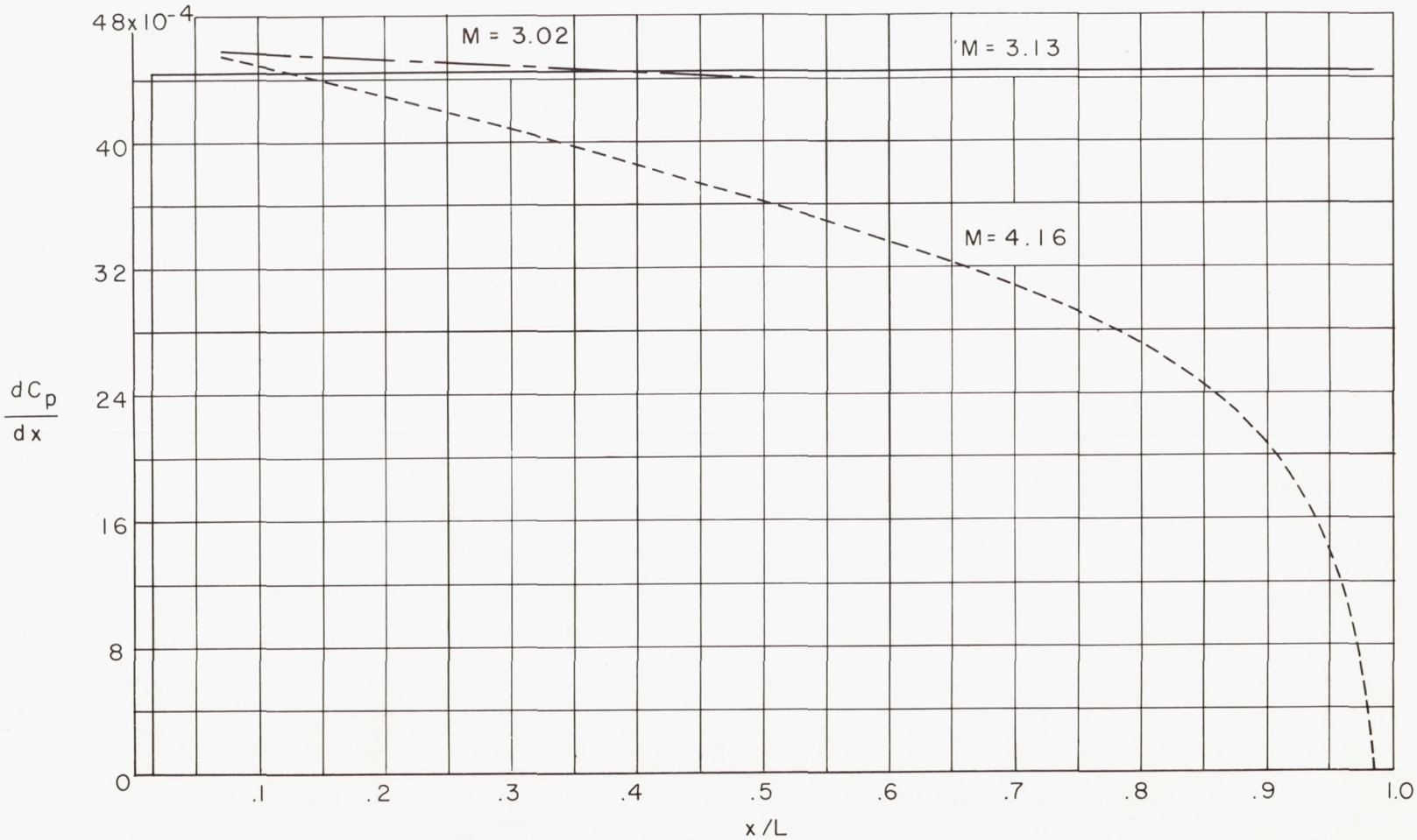

Figure 7.- Variation of dC_p/dx for linear constant-pressure-gradient body at designed condition of $M_\infty = 3.13$ and off-design condition of $M_\infty = 3.02$ and $M_\infty = 4.16$.

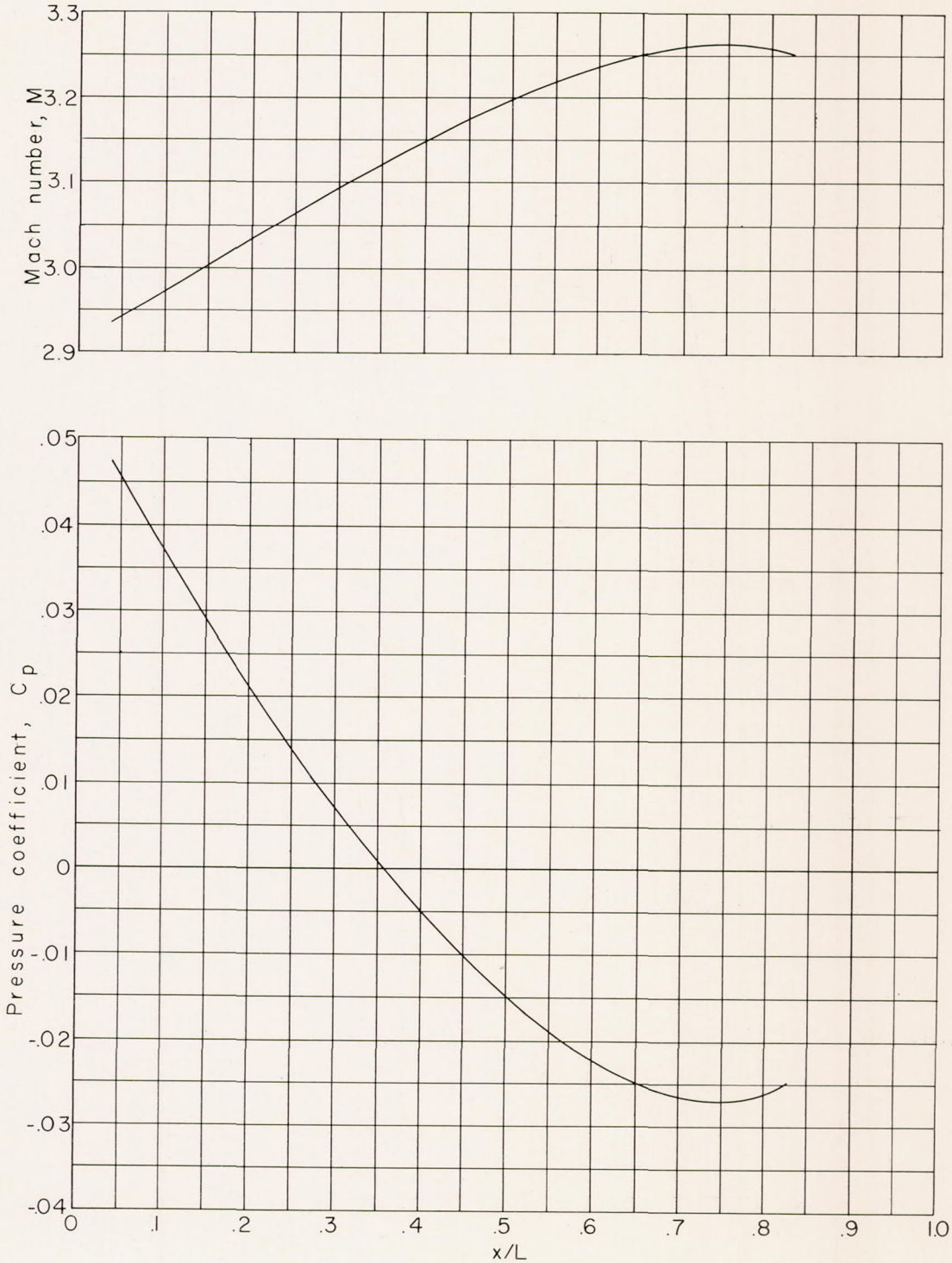

Figure 8.- Distribution of M and C_p for NACA RM-10 research missile at $M_\infty = 3.12$.

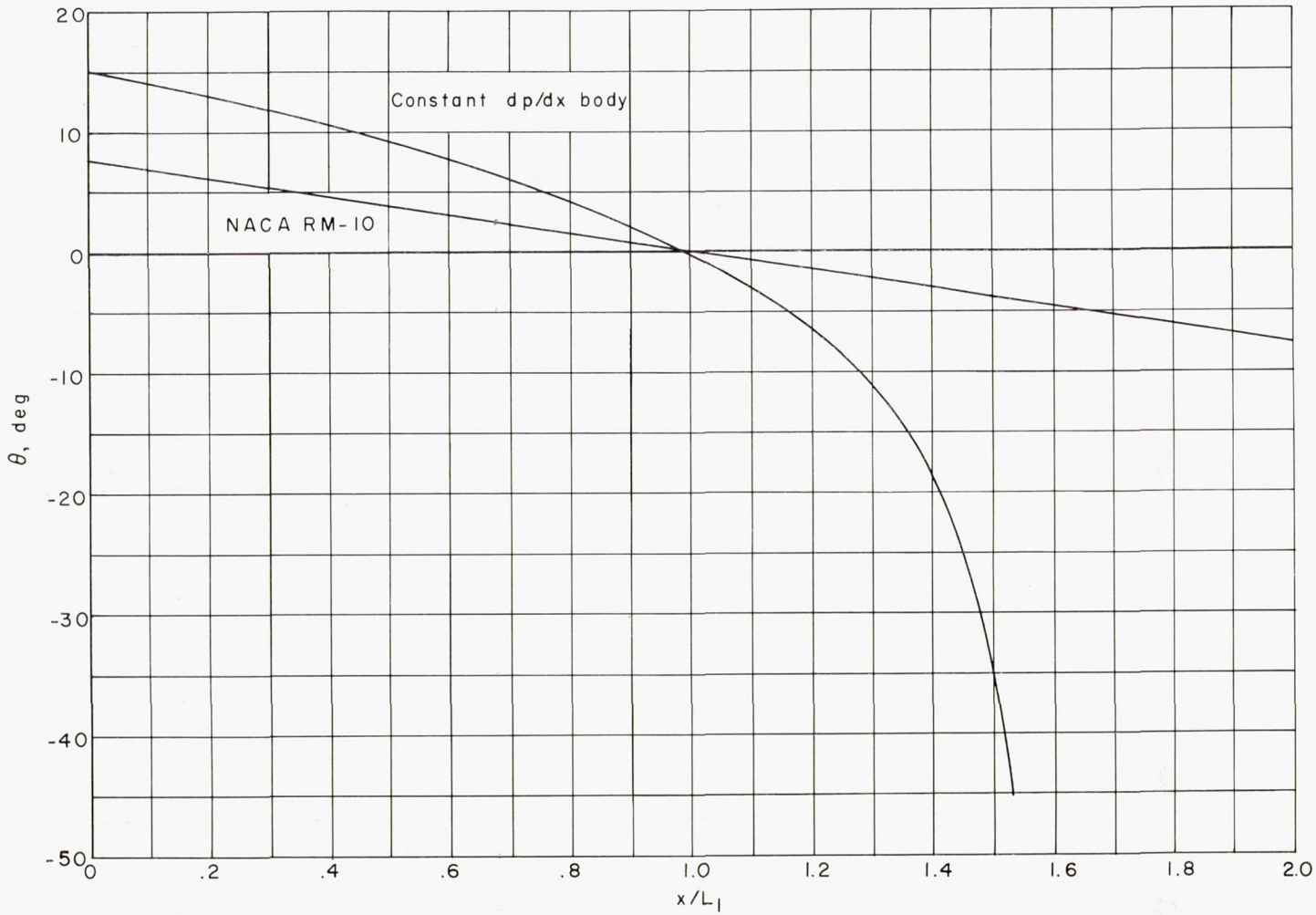

Figure 9.- Comparison of slope of surface of the NACA RM-10 missile and the constant-pressure-gradient model.

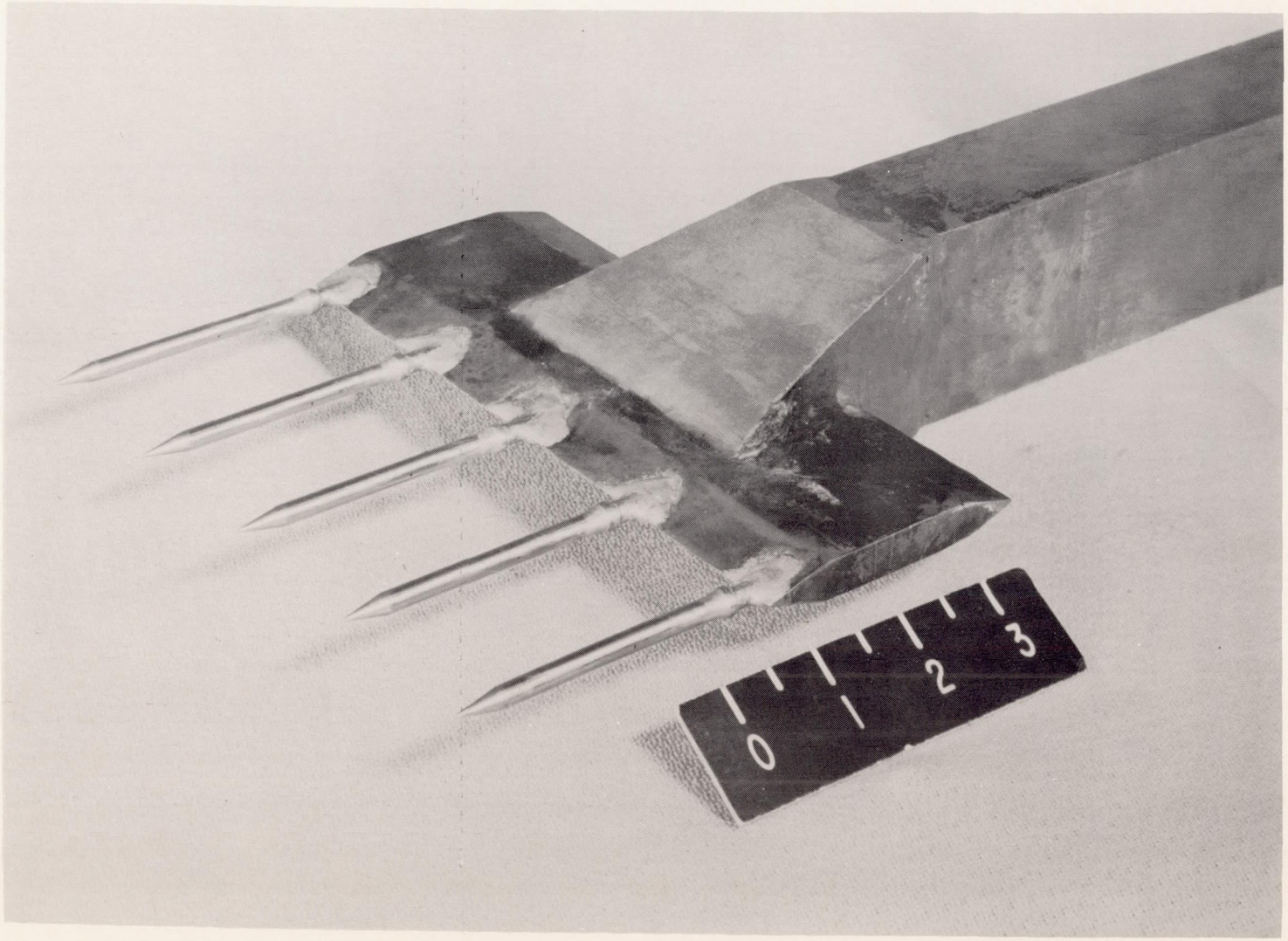

Figure 10.- Multitube static-pressure rake for nozzle calibrations. L-84206

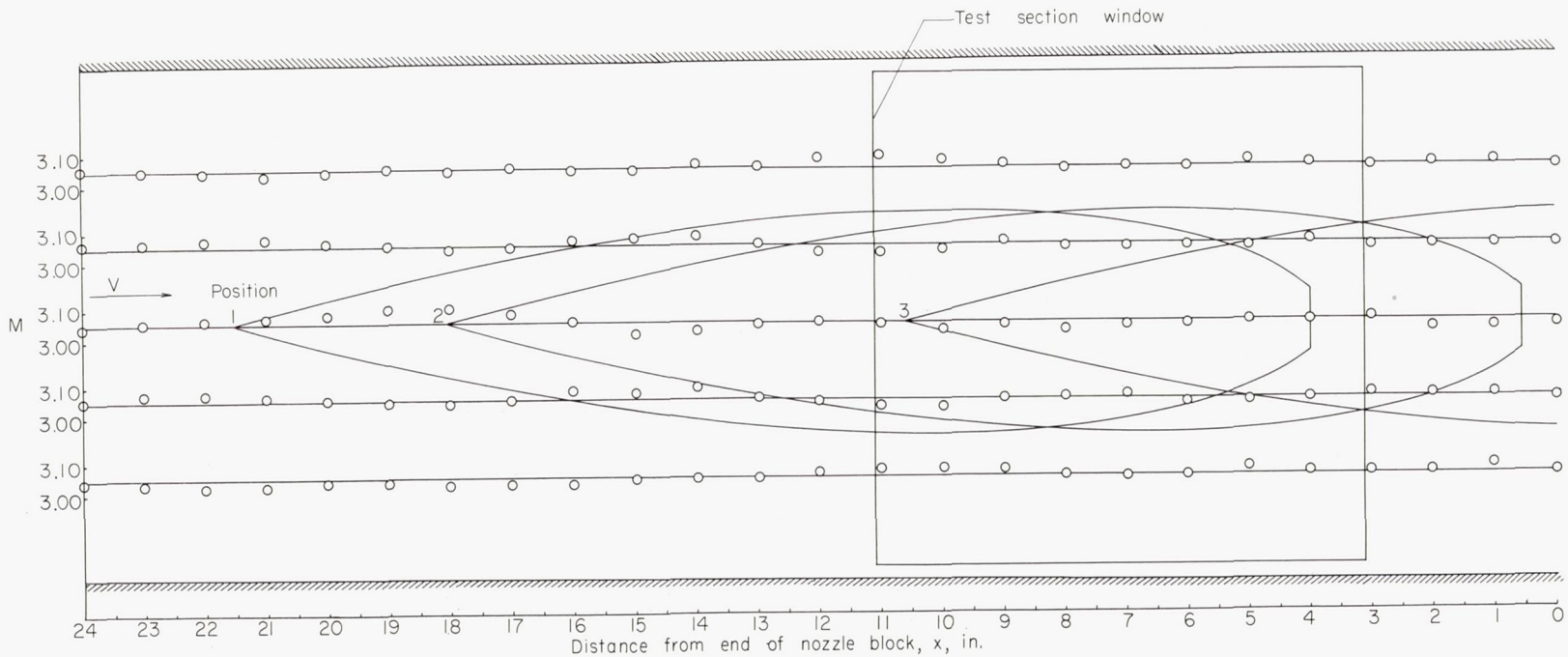

Figure 11.- Nozzle calibration for $M = 3.05$ at a Reynolds number per inch of 2.77×10^6.

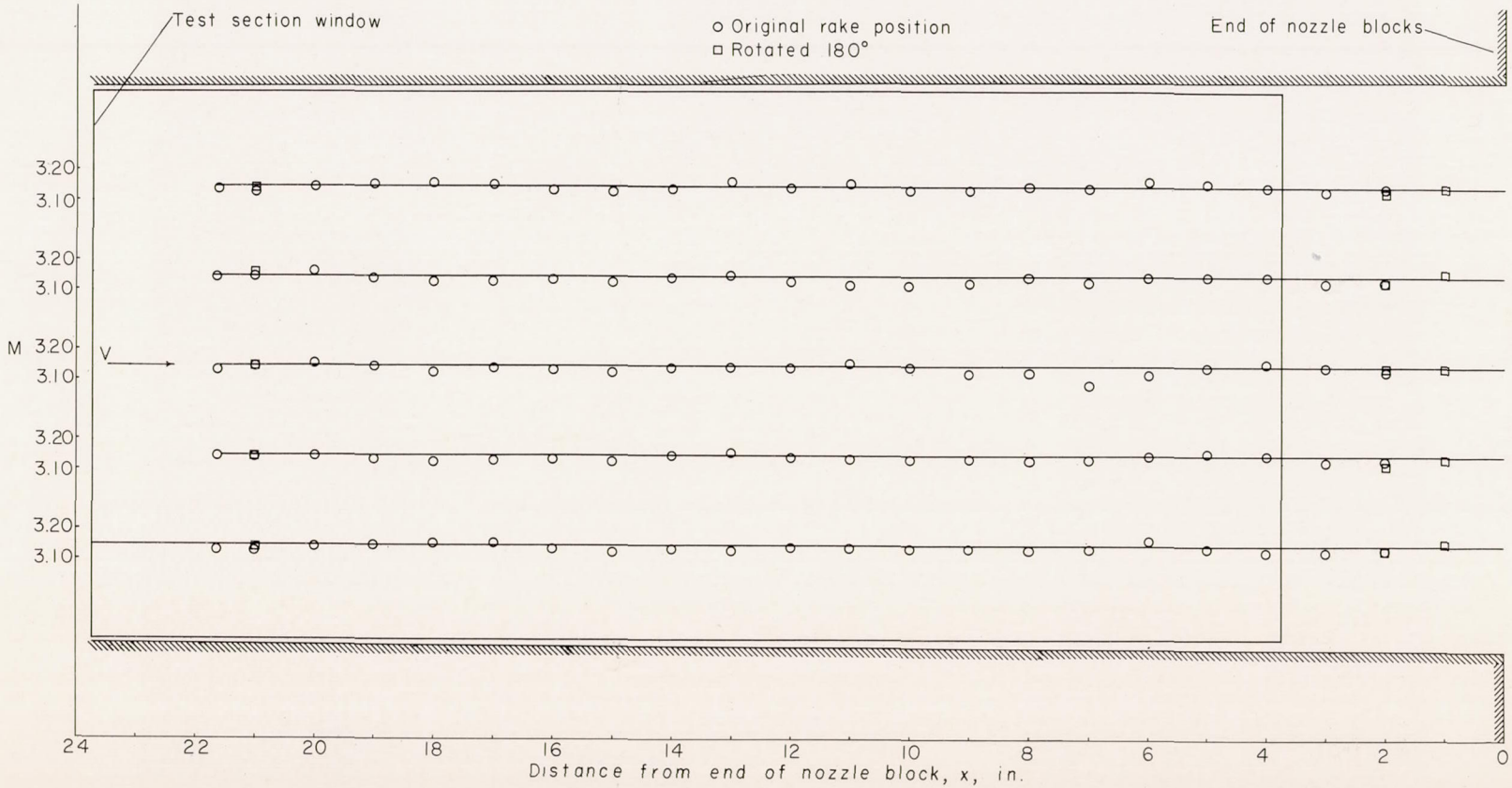

Figure 12.- Nozzle calibration for $M = 3.13$ at a Reynolds number per inch of 2.64×10^6.

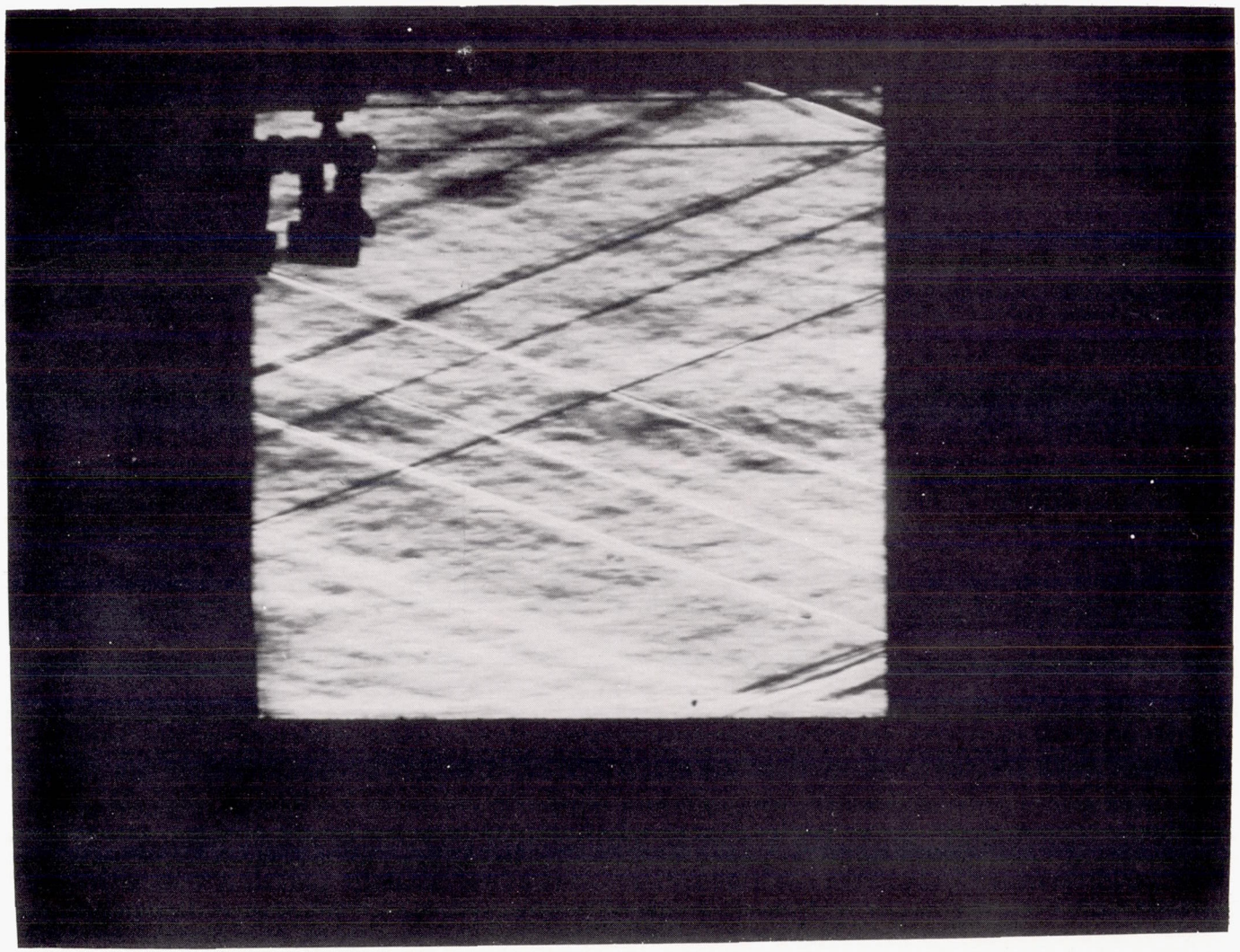

Figure 13.- Schlieren photograph of $M = 3.05$ test section.

L-90512

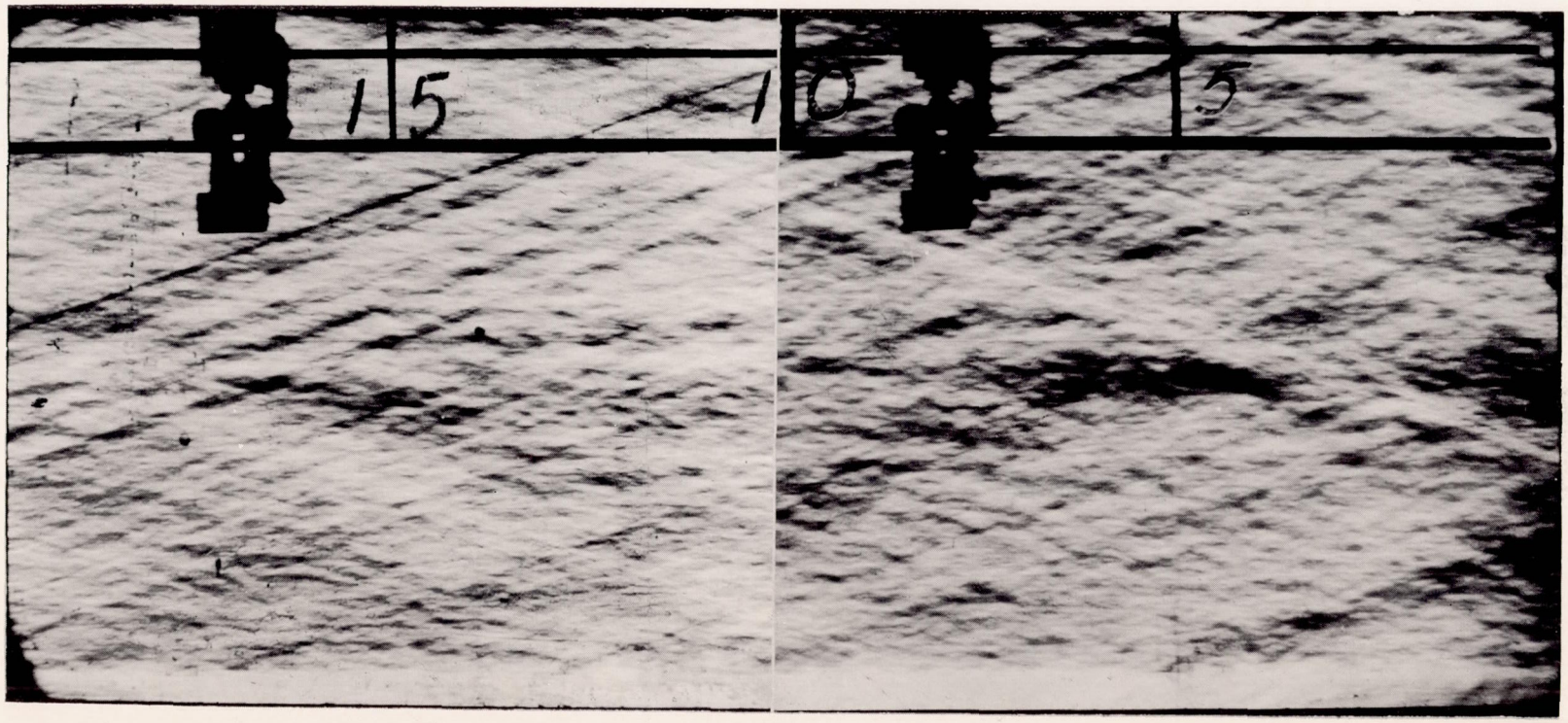

Figure 14.- Composite schlieren photograph of $M = 3.13$ test section. L-90513

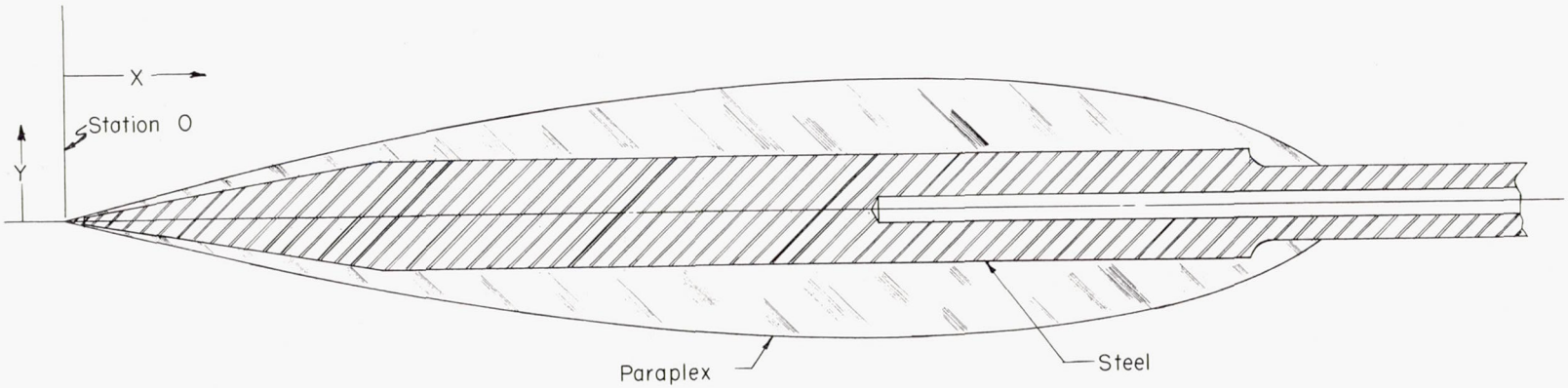

x, in.	y, in.	x, in.	y, in.	x, in.	y, in.
0	0	8.0	1.587	13.75	1.697
.5	.137	8.5	1.639	14.0	1.670
1.0	.263	9.0	1.686	14.25	1.638
1.5	.387	9.5	1.726	14.5	1.603
2.0	.509	10.0	1.758	14.75	1.562
2.5	.627	10.5	1.783	15.0	1.517
3.0	.739	11.0	1.798	15.25	1.467
3.5	.846	11.5	1.804	15.5	1.409
4.0	.949	11.75	1.804	15.75	1.344
4.5	1.047	12.0	1.798	16.0	1.272
5.0	1.141	12.25	1.793	16.25	1.189
5.5	1.230	12.5	1.785	16.5	1.098
6.0	1.313	12.75	1.775	16.75	.991
6.5	1.391	13.0	1.761	17.0	.874
7.0	1.462	13.25	1.743	17.25	.727
7.5	1.527	13.5	1.723	17.5	.554
				17.75	.325

Figure 15.- Sketch of constant-pressure-gradient model with pertinent dimensions.

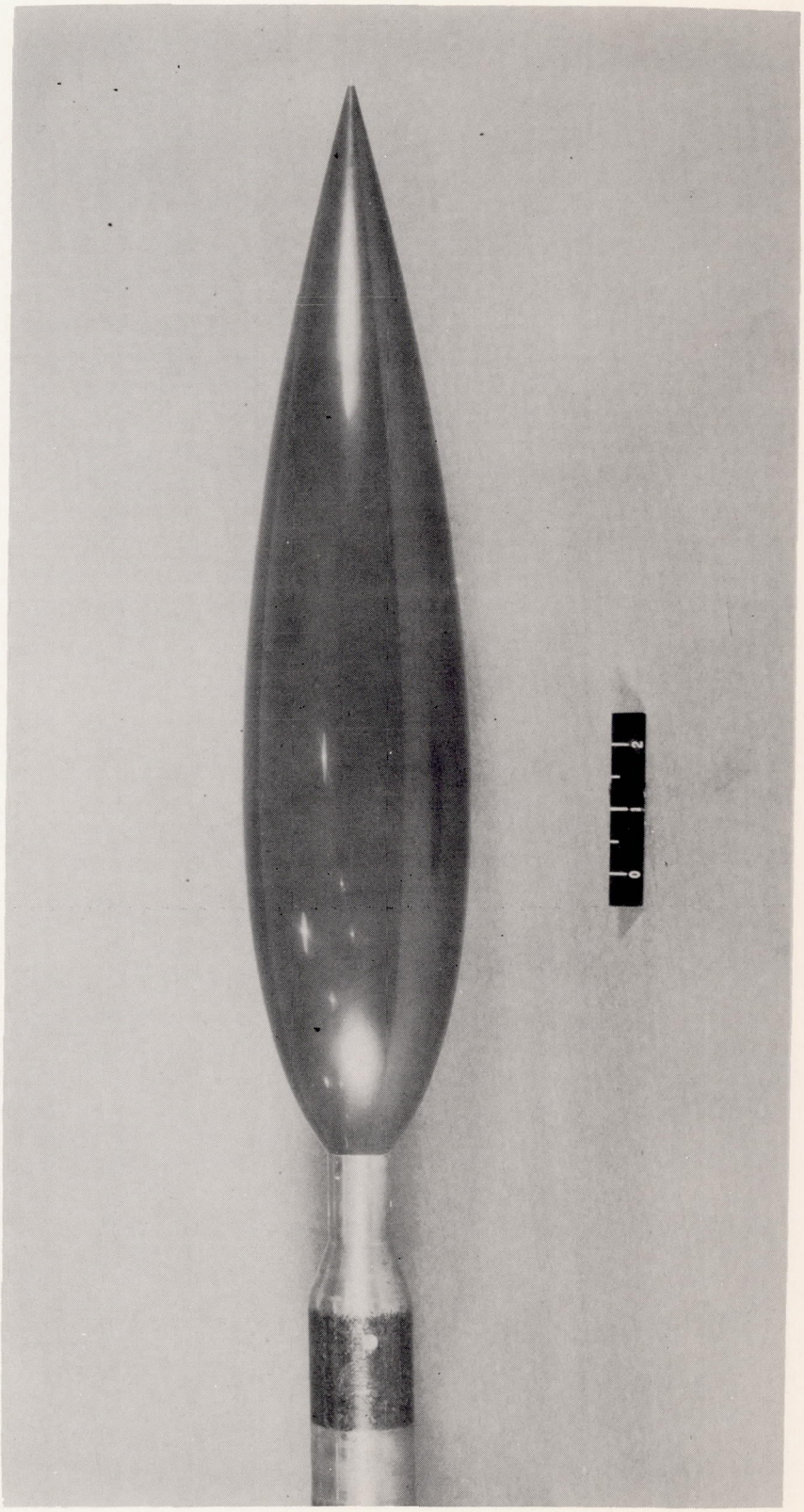

L-80691

Figure 16.- Photograph of constant-pressure-gradient body.

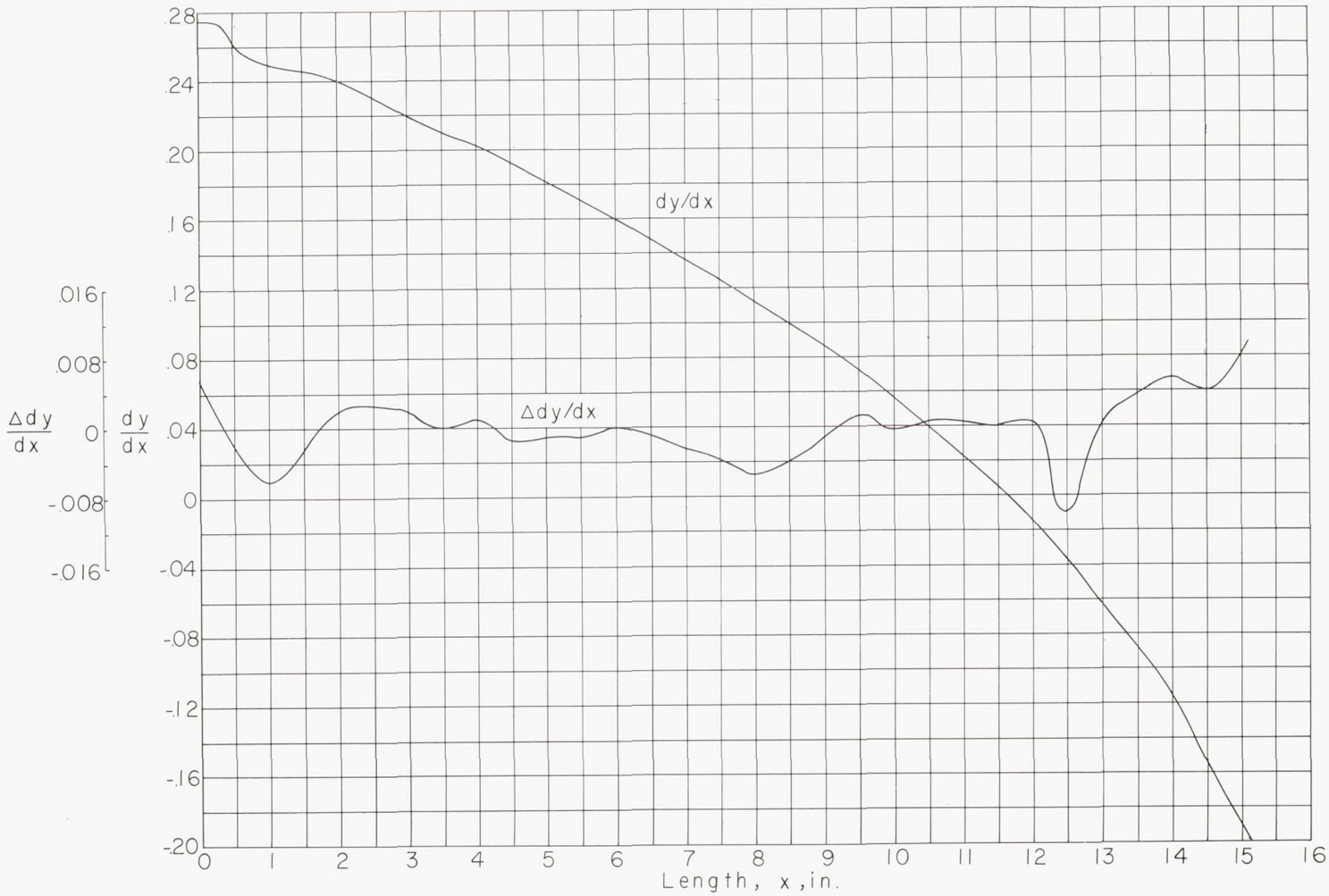

Figure 17.- Design slope for the contour of the model and deviation of the experimental model from design.

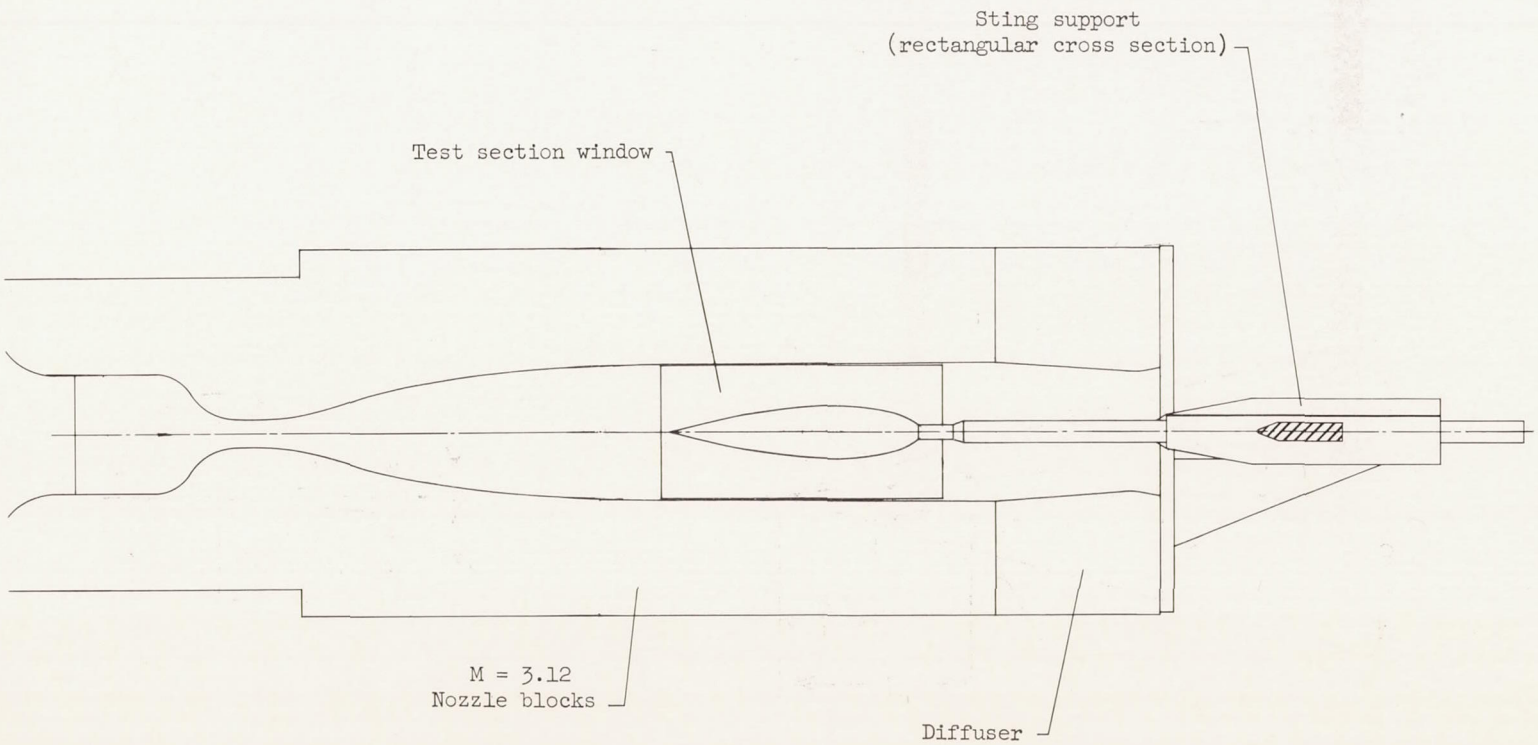

Figure 18.- Sketch of model in M = 3.13 tunnel.

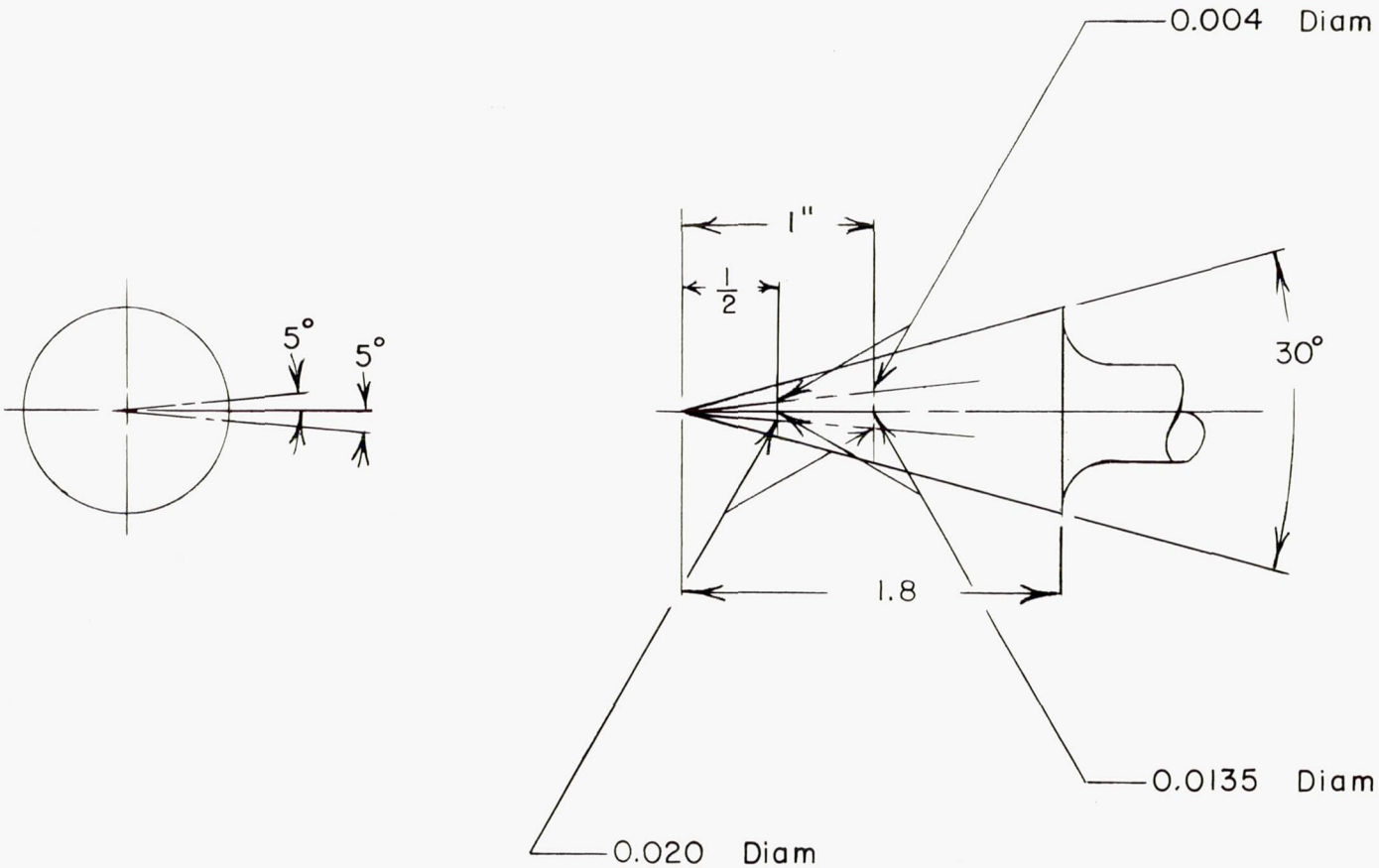

Figure 19.- Sketch of cone used in orifice investigation.

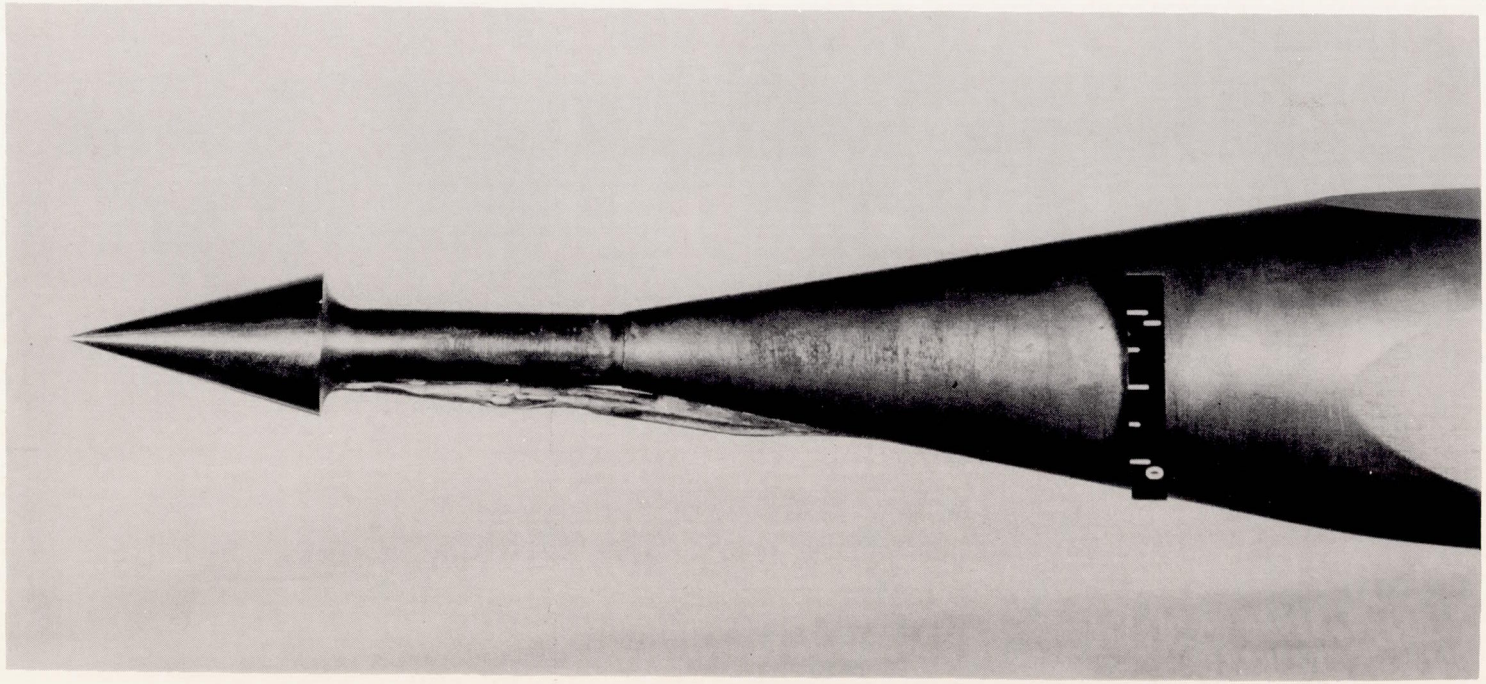

Figure 20.- Photograph of cone used in orifice investigation. L-84387

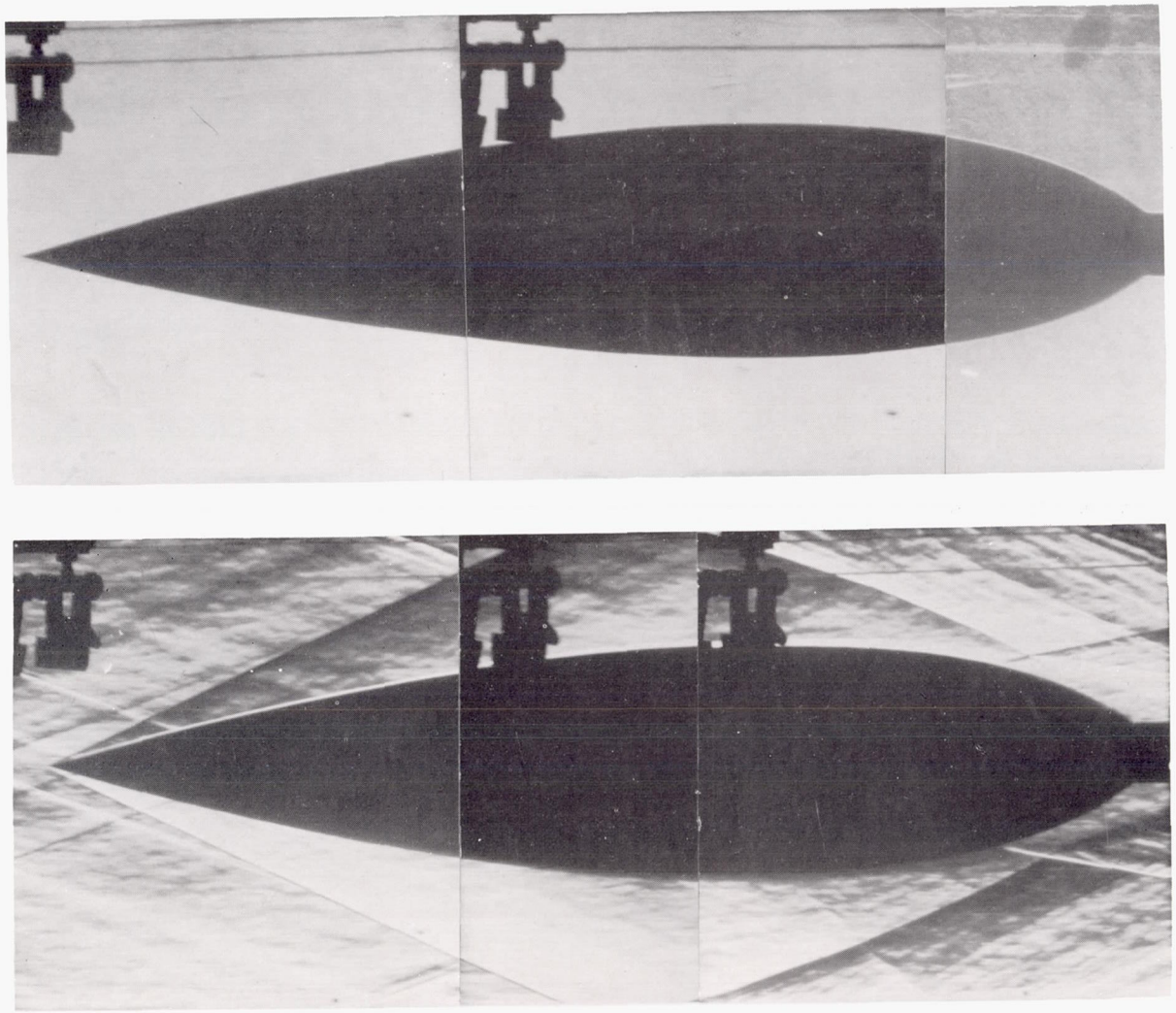

L-90514

Figure 21.- Composite schlieren photographs of constant-pressure-gradient model at $M = 3.05$ for Reynolds numbers of 0 and 48.6×10^6.

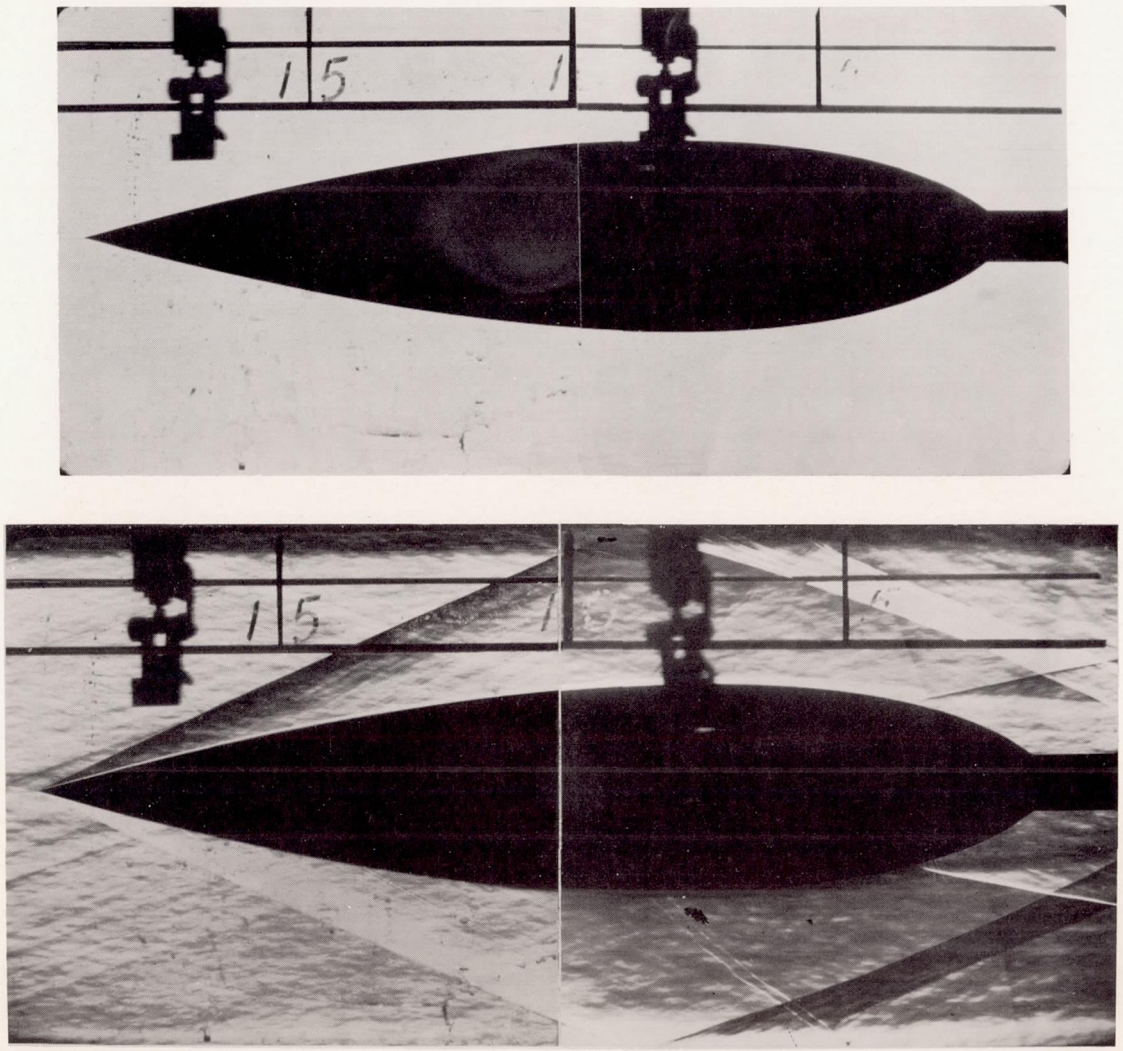

L-90515

Figure 22.- Composite schlieren photograph of model at $M = 3.13$ for Reynolds numbers of 0 and 46.2×10^6.

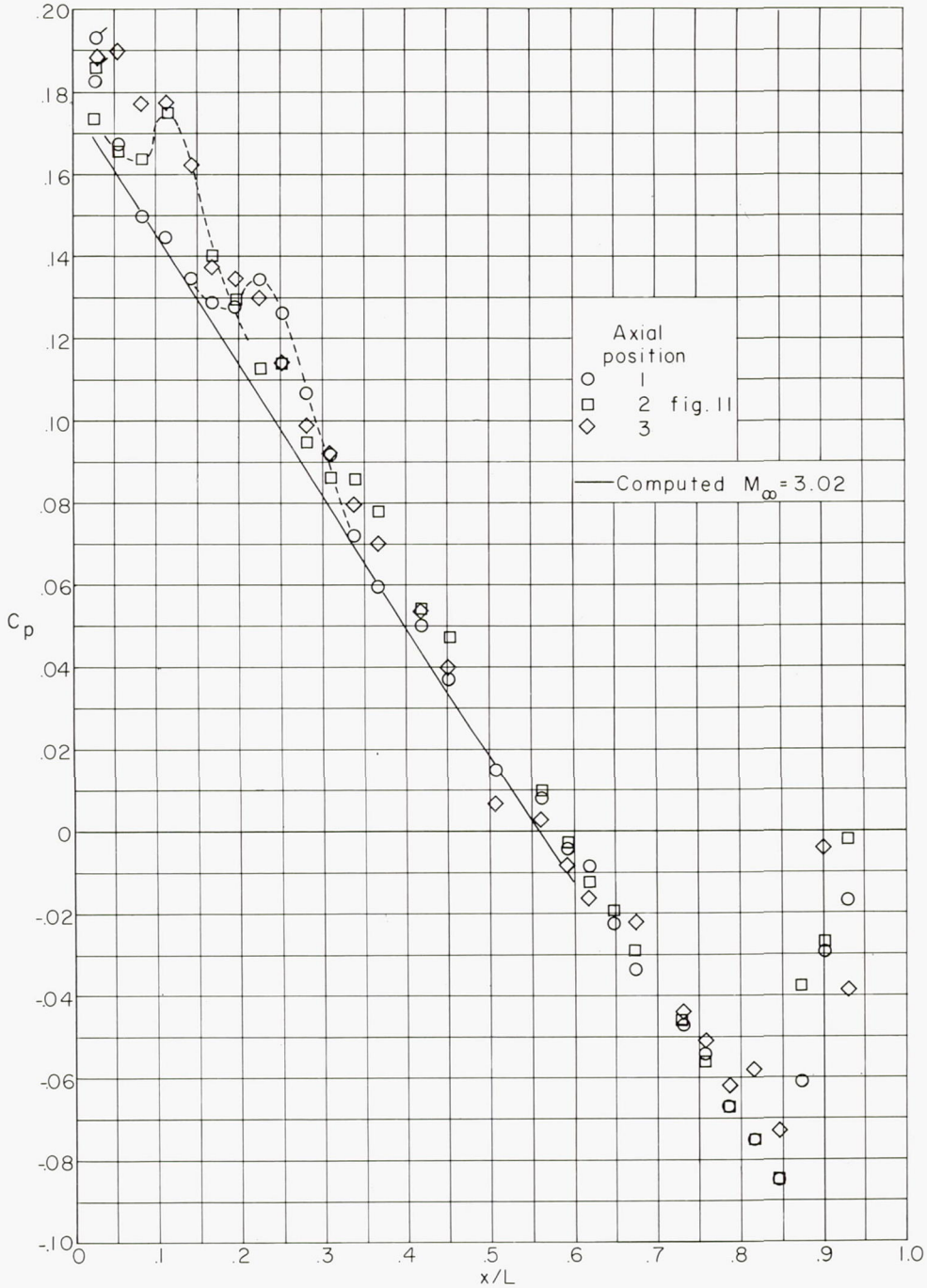

(a) Effect of varying axial position of model in tunnel at Reynolds number 48.6×10^6 with orifice at 0°.

Figure 23.- Axial distribution of pressure coefficient of constant-pressure-gradient body at $M_\infty = 3.05$. Flagged symbols denote orifice displaced 180°. Dashed lines indicate the effect of the compression.

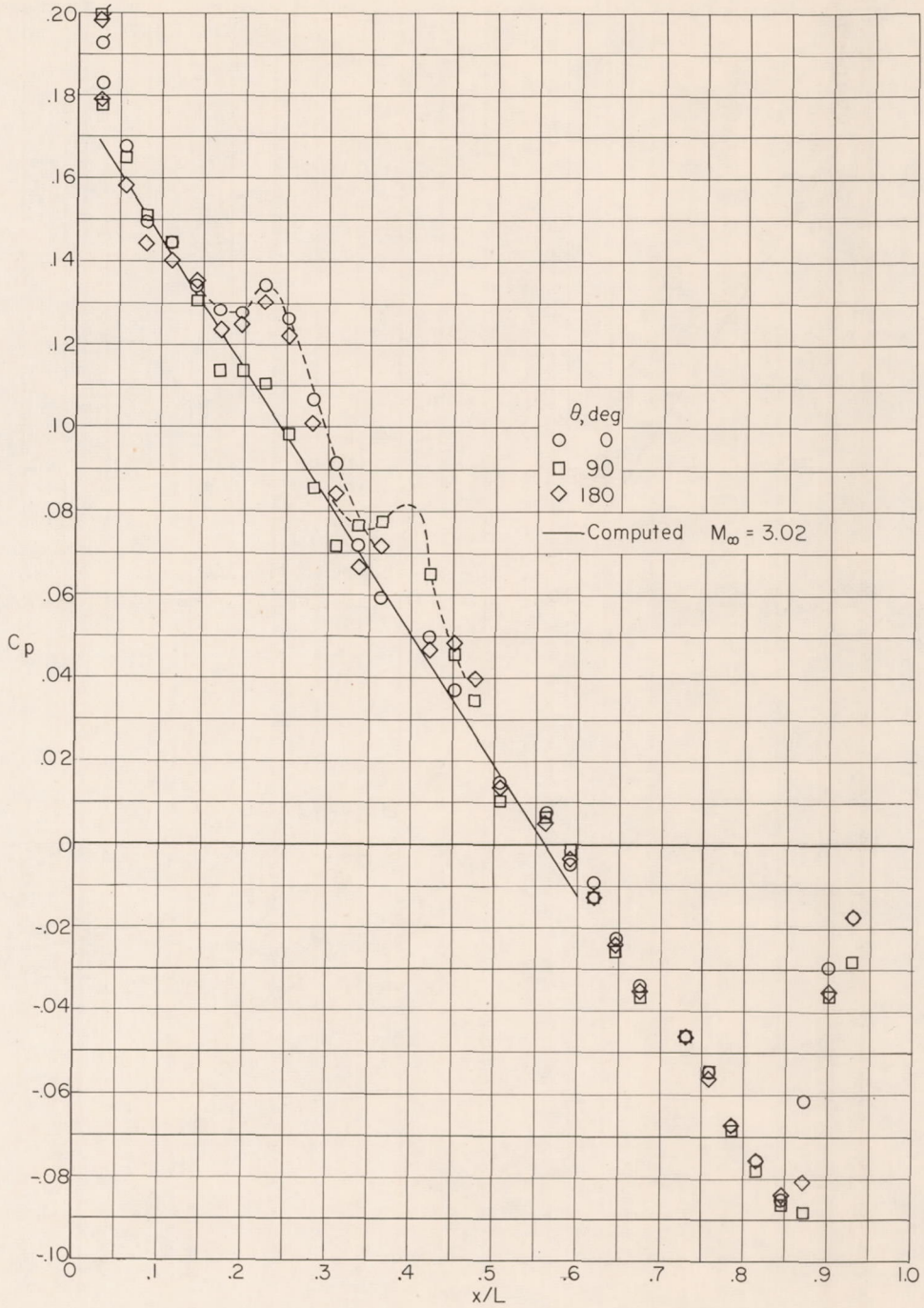

(b) Effect of radial position of the orifices with the model at position 1 in tunnel at Reynolds number 48.6×10^6.

Figure 23.- Continued.

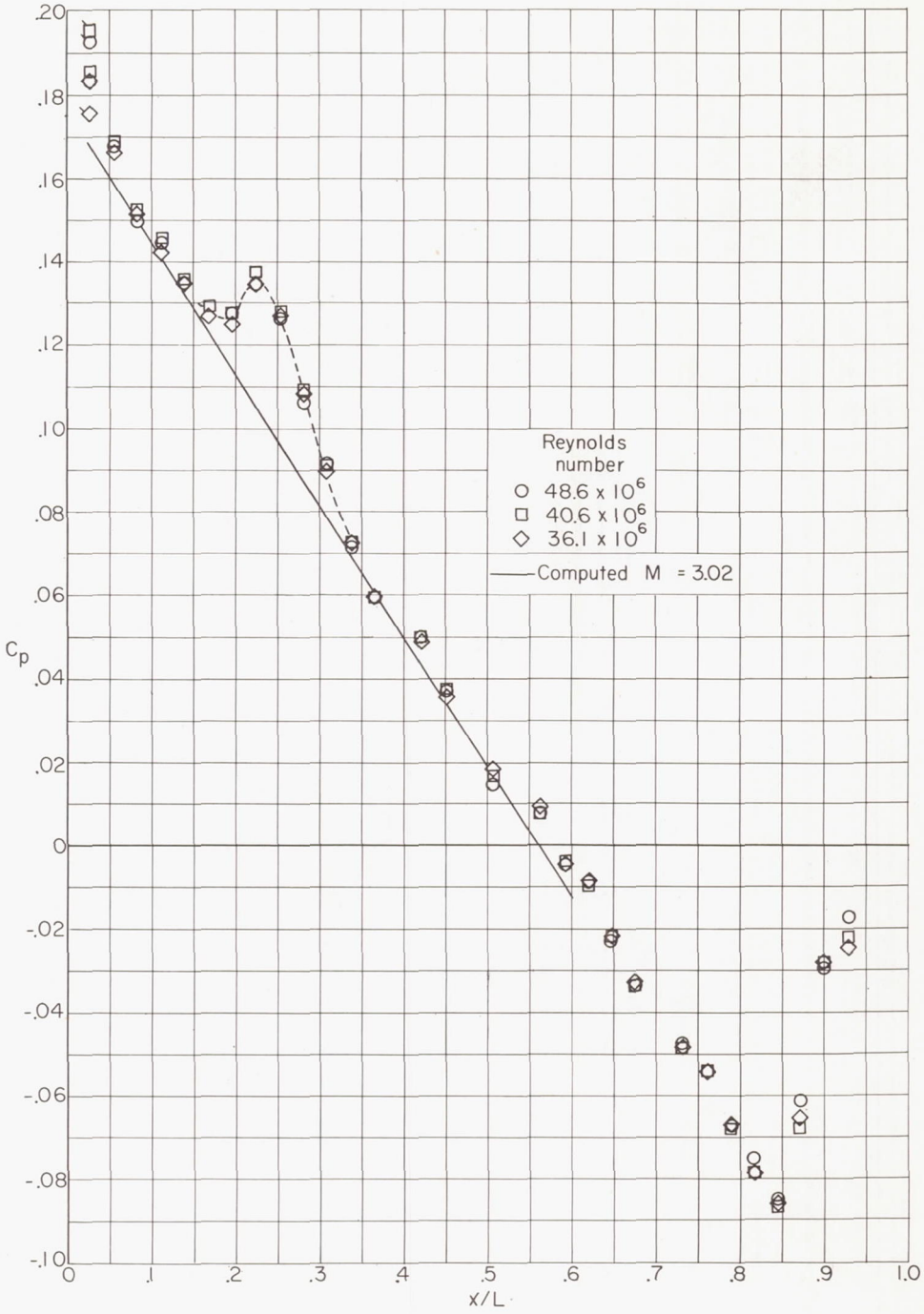

(c) Effect of varying Reynolds number with the orifices at 0° at position 1.

Figure 23.- Concluded.

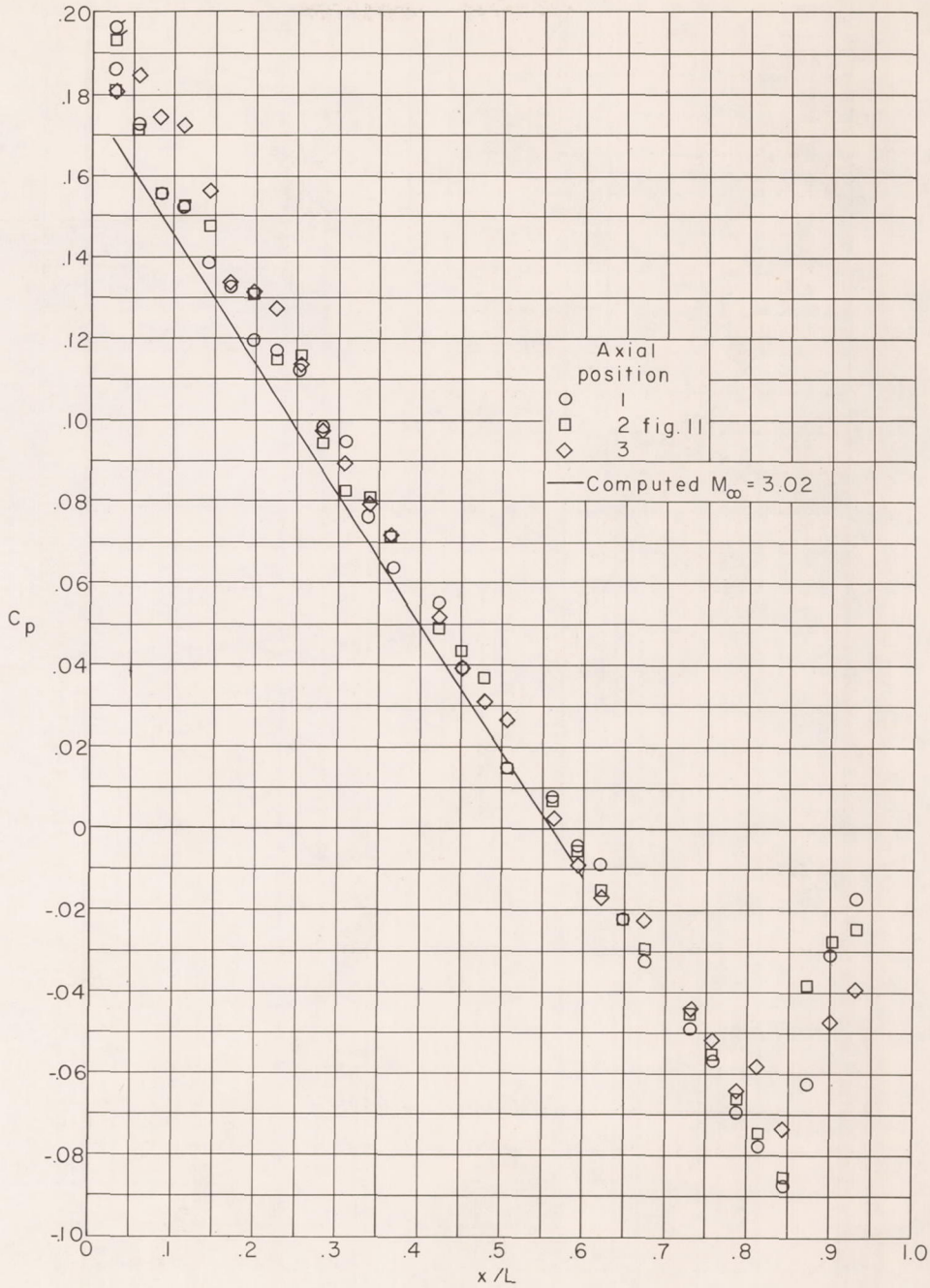

(a) Effect of varying axial position of model in tunnel at Reynolds number 48.6×10^6 corrected for free-stream disturbances.

Figure 24.- Axial distribution of pressure coefficient of constant-pressure-gradient body at $M_\infty = 3.05$ corrected for free-stream disturbances. Flagged symbols denote orifice displaced 180°.

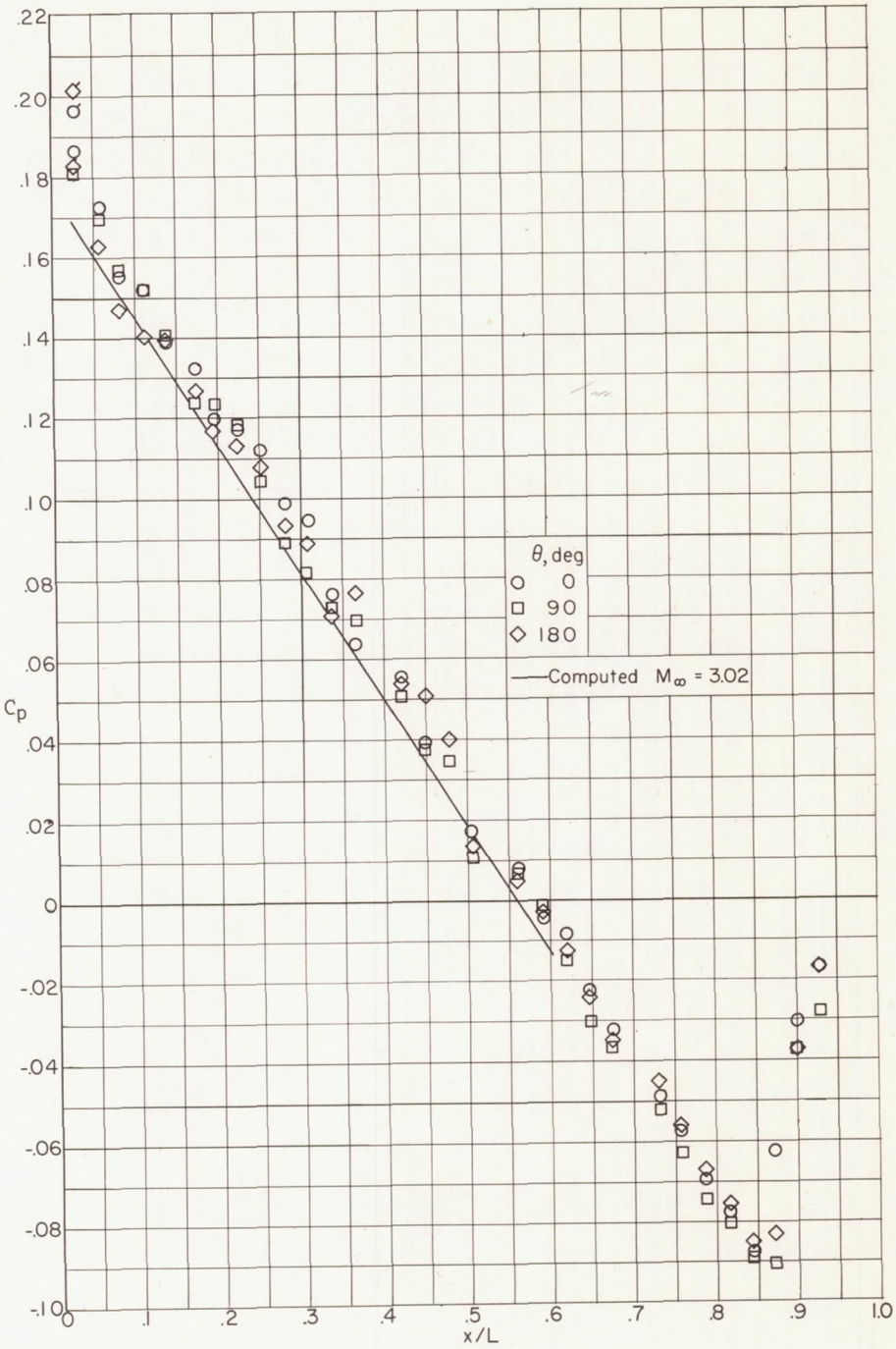

(b) Effect of radial position of the orifices with the model at position 1 in tunnel at Reynolds number 48.6×10^6 corrected for free-stream disturbances.

Figure 24.- Continued.

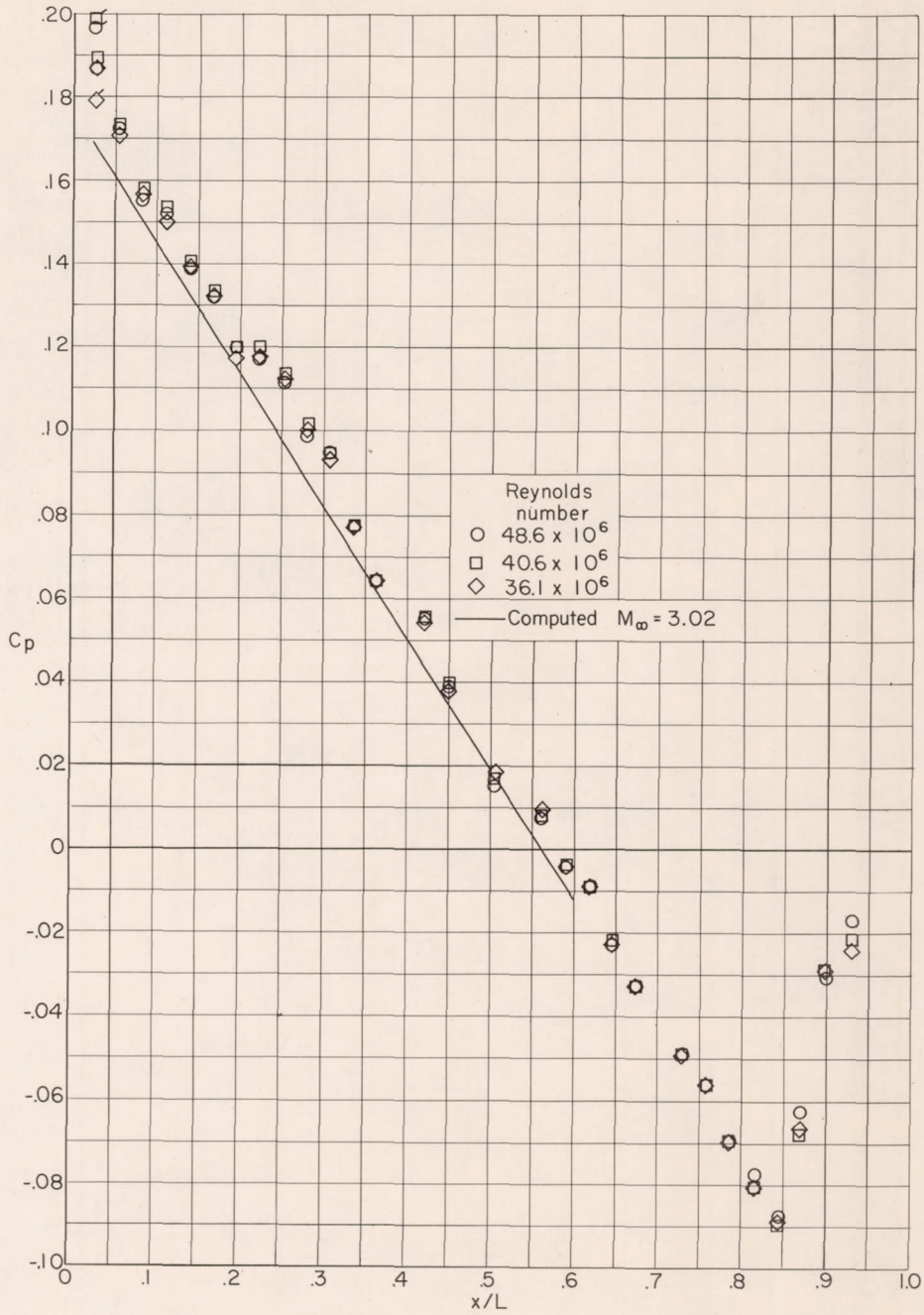

(c) Effect of varying Reynolds number with the orifices at 0° at position 1 corrected for free-stream disturbances.

Figure 24.- Concluded.

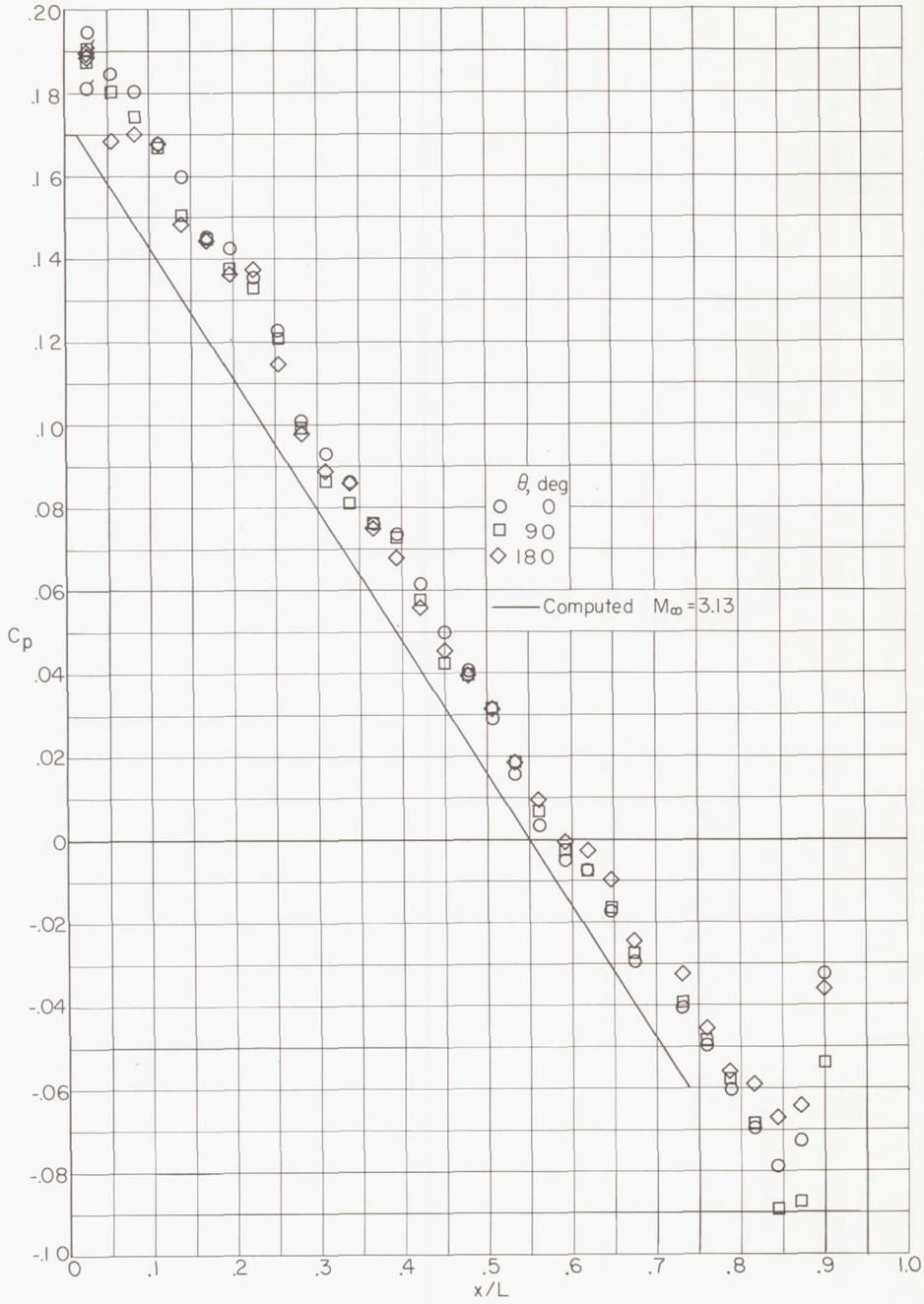

(a) Effect of radial position of orifices at Reynolds number 46.2×10^6.

Figure 25.- Axial distribution of pressure coefficient of constant-pressure-gradient body at $M_\infty = 3.13$ corrected for free-stream disturbances. Flagged symbols denote orifice displaced 180°.

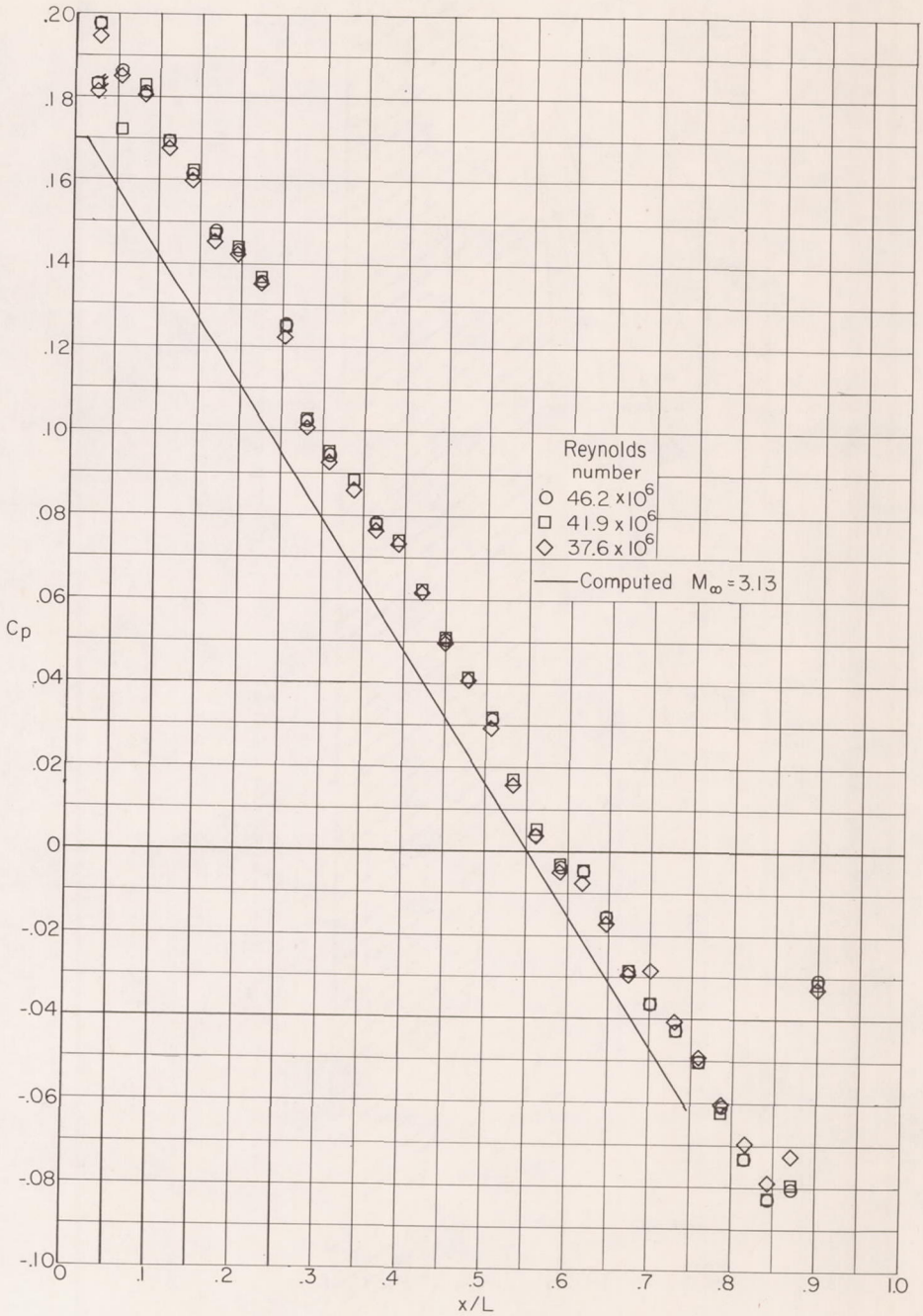

(b) Effect of varying Reynolds number with orifices at 0°.

Figure 25.- Concluded.

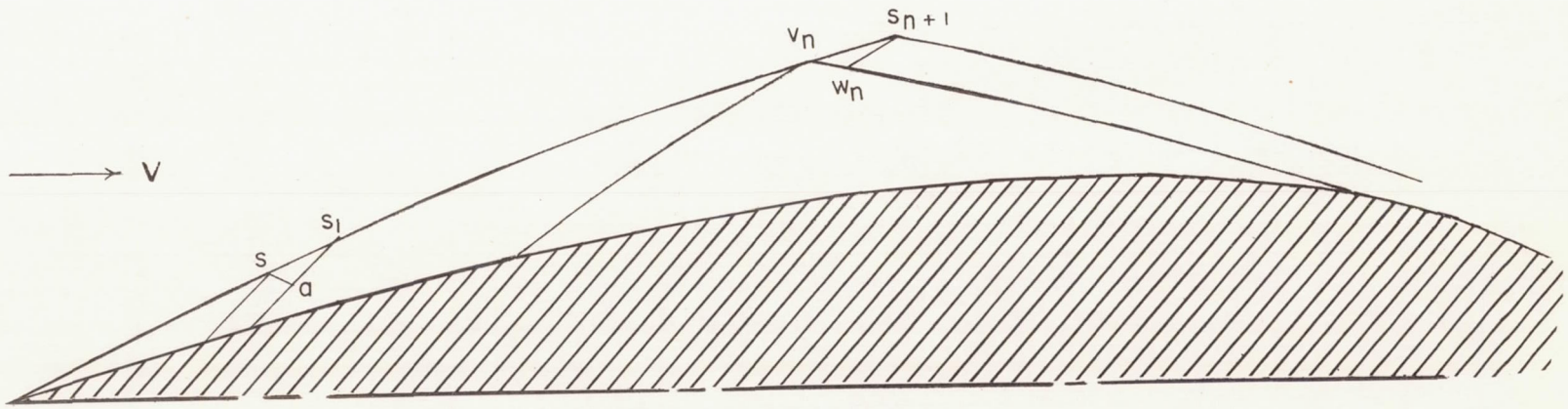

Figure 26.- Sketch of characteristic net for computing $dw/d\delta$.

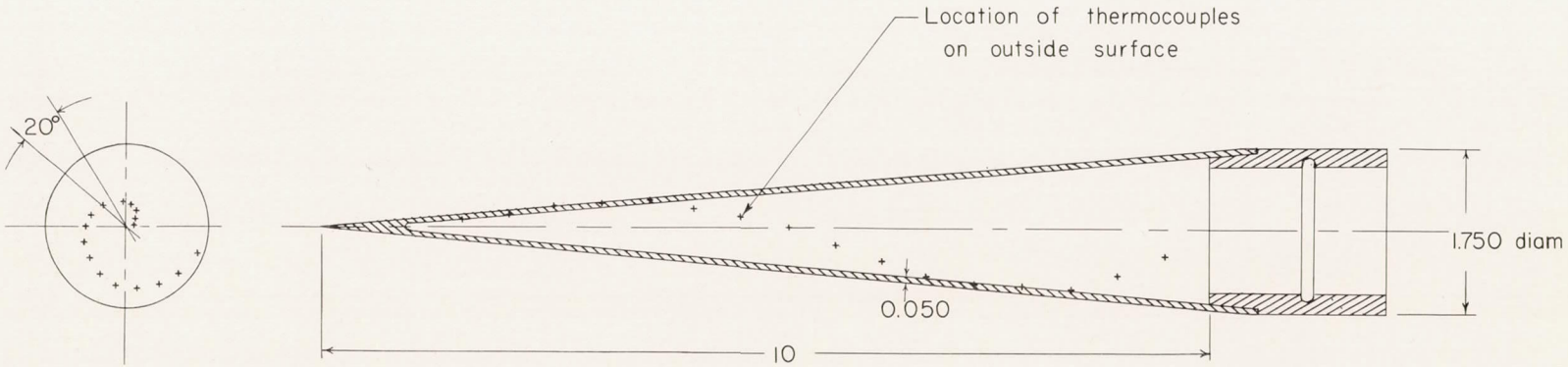

Figure 27.- Sketch of the model used for the transition investigation.

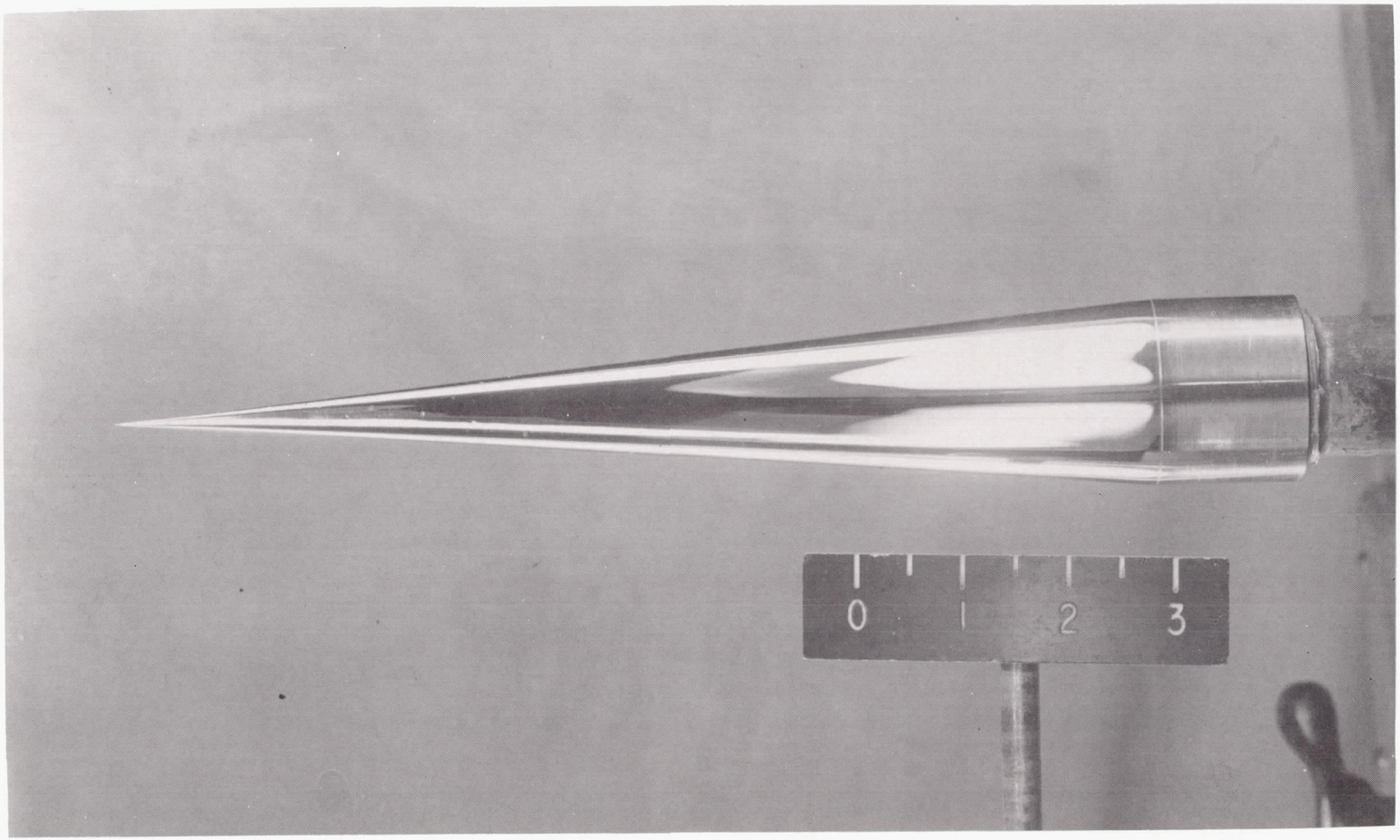

L-87672

Figure 28.- Photograph of 10° cone used for transition investigation.

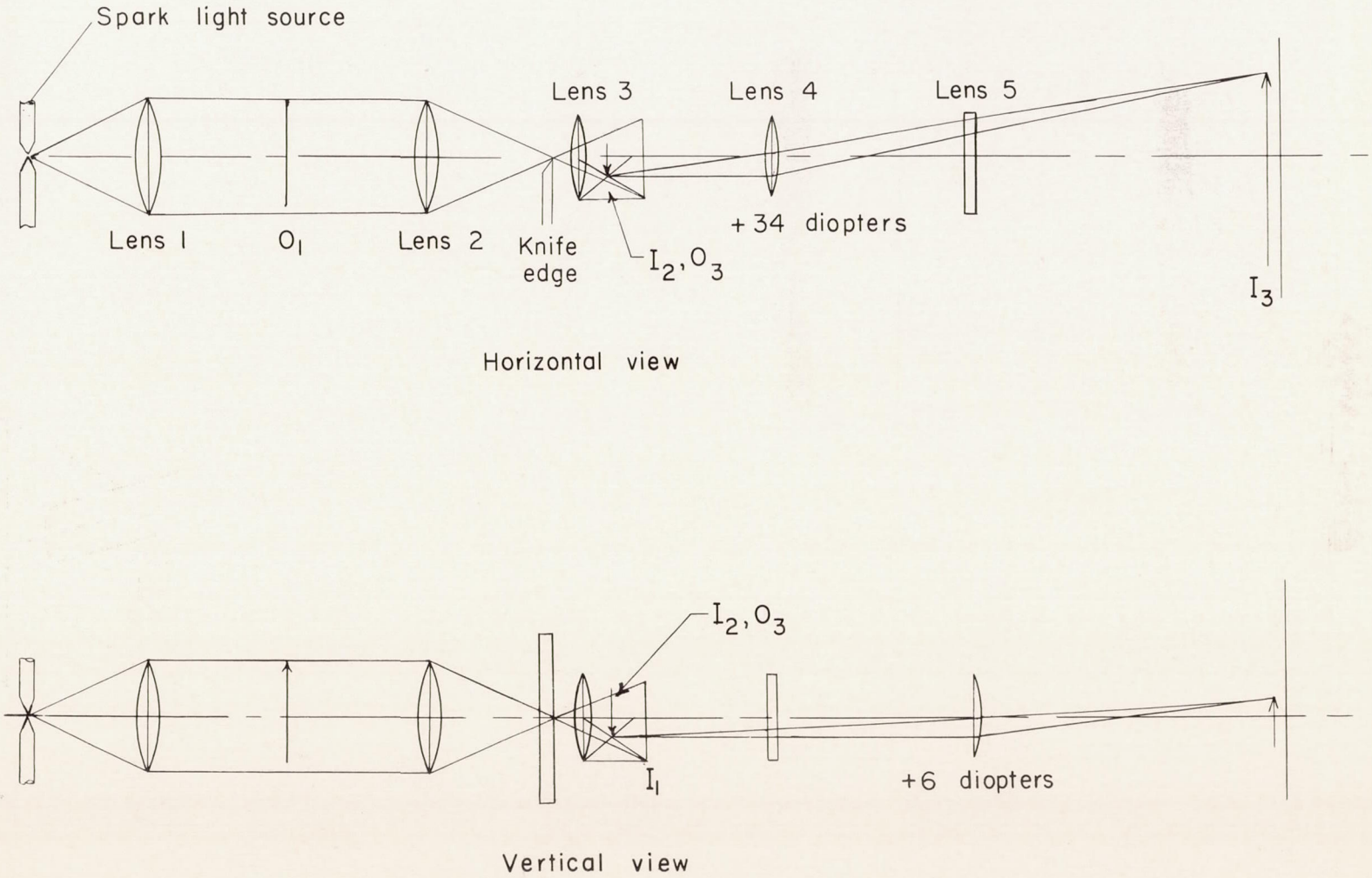

Figure 29.- Optical lens system for producing greater magnification in a plane normal to the flow.

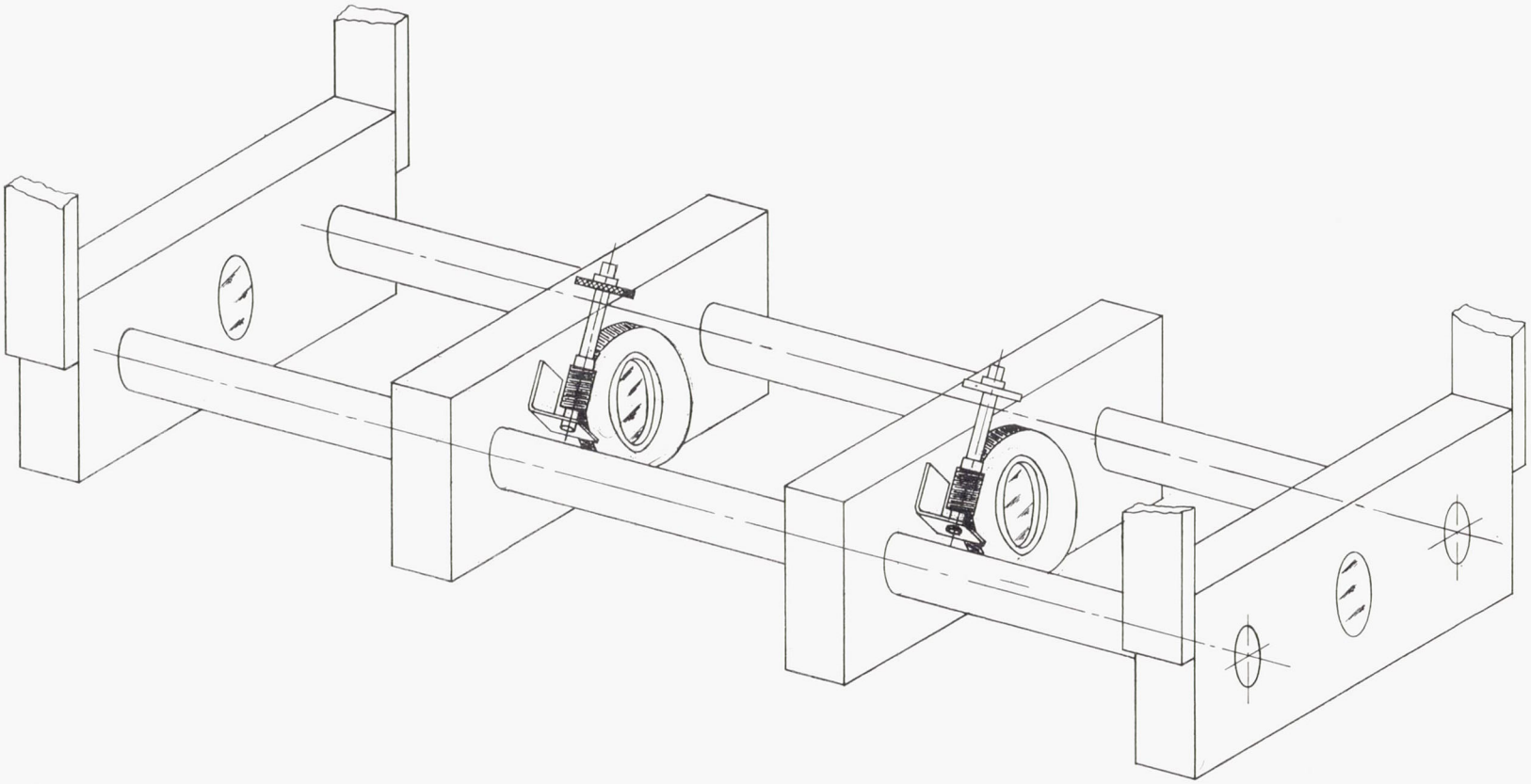

Figure 30.- Lens mount for producing unequal magnification of schlierens.

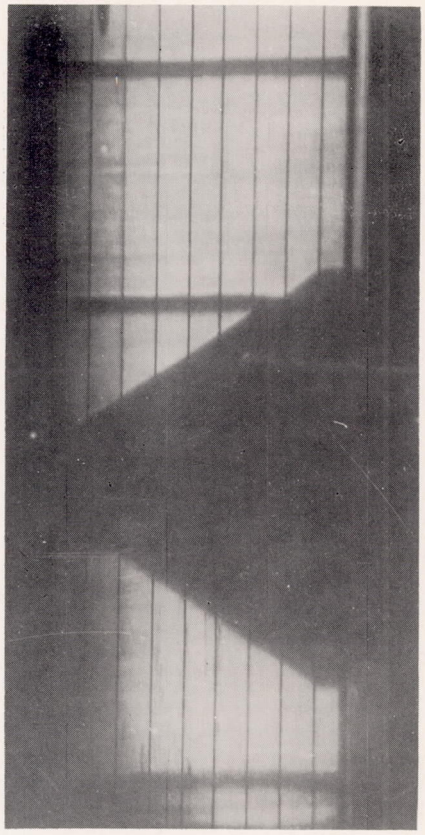

(a) Asymmetrical.

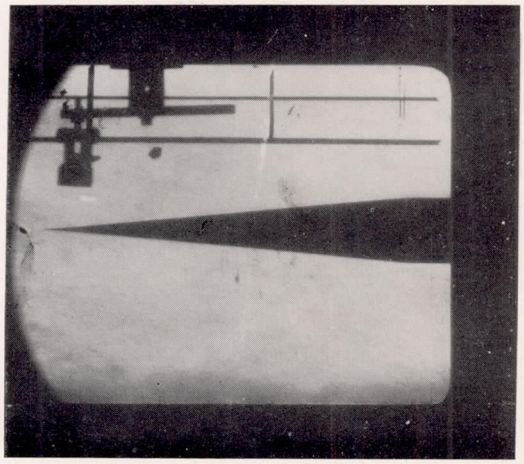

(b) Conventional.

L-90516

Figure 31.- Comparison of 10° cone using conventional and asymmetrical schlierens.

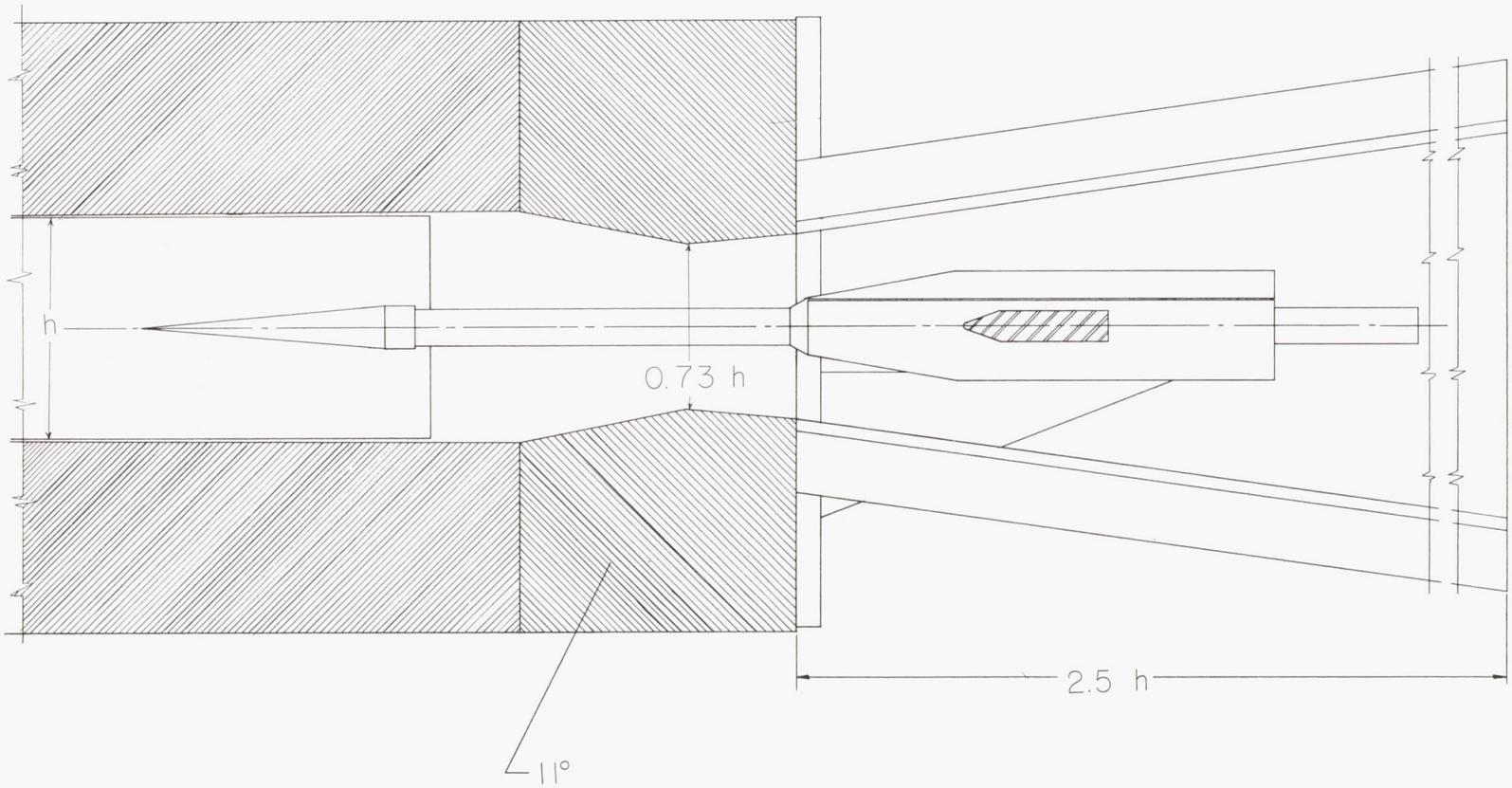

Figure 32.- Sketch of model and diffuser for transition tests.

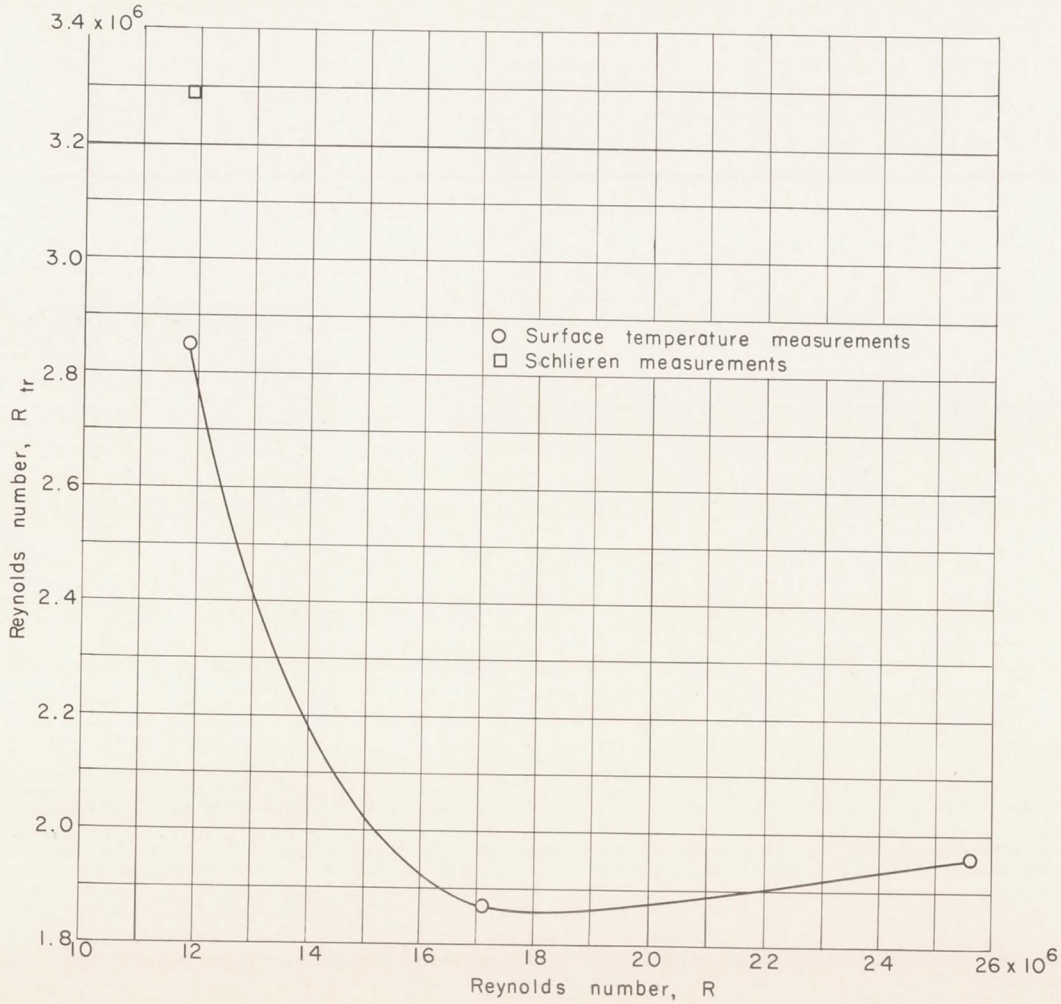

Figure 33.- Variation of transitional Reynolds number with stream Reynolds number measured with a 10° cone.

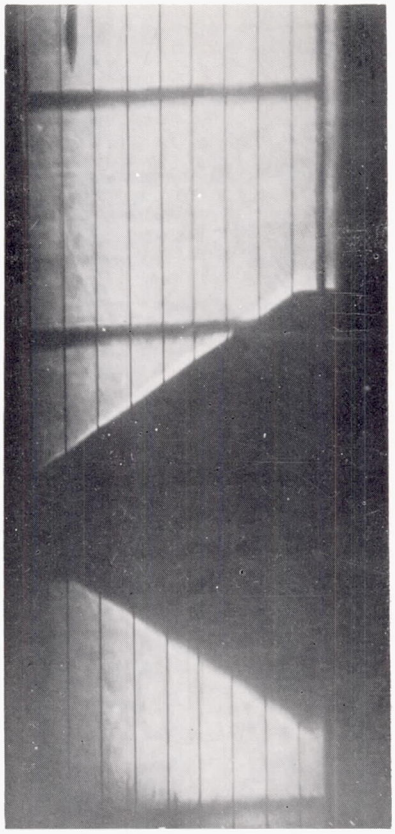

(a) Asymmetrical.

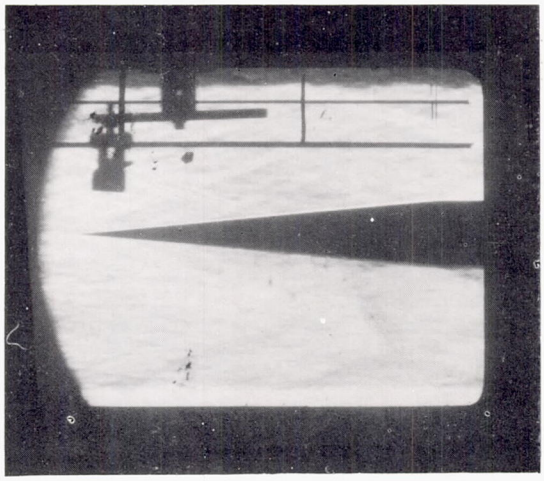

(b) Conventional.

L-90517

Figure 34.- Comparison of conventional and asymmetrical schlierens on a 10° cone at $R = 12 \times 10^{6}$.